

CHEMical complexity in star-forming regions of the OUTER Galaxy (CHEMOUT). II. Methanol formation at low metallicity

F. Fontani^{1, 2}, A. Schmiedeke², A. Sánchez-Monge³, L. Colzi^{4, 1}, D. Elia⁵, V.M. Rivilla^{4, 1}, M.T. Beltrán¹, L. Bizzocchi^{6, 2}, P. Caselli², L. Magrini¹, and D. Romano⁷

¹ INAF-Osservatorio Astrofisico di Arcetri, Largo E. Fermi 5, I-50125, Florence, Italy

e-mail: francesco.fontani@inaf.it

² Centre for Astrochemical Studies, Max-Planck-Institute for Extraterrestrial Physics, Giessenbachstrasse 1, 85748 Garching, Germany

³ I. Physikalisches Institut, Universität zu Köln, Zùlpicher Str. 77, 50937 Köln, Germany

⁴ Centro de Astrobiología (CSIC-INTA), Ctra. de Ajalvir Km. 4, Torrejón de Ardoz, 28850 Madrid, Spain

⁵ INAF - IAPS, via Fosso del Cavaliere, 100, I-00133 Roma, Italy

⁶ Dipartimento di Chimica "Giacomo Ciamician", Università di Bologna, Bologna, Italy

⁷ INAF, Osservatorio di Astrofisica e Scienza dello Spazio, Via Gobetti 93/3, 40129, Bologna, Italy

Received ; accepted

ABSTRACT

Context. The outer Galaxy is an environment with metallicity lower than the Solar one and, because of this, the formation and survival of molecules in star-forming regions located in the inner and outer Galaxy is expected to be different.

Aims. To gain understanding on how chemistry changes throughout the Milky Way, it is crucial to observe outer Galaxy star-forming regions to constrain models adapted for lower metallicity environments.

Methods. The project "chemical complexity in star-forming regions of the outer Galaxy" (CHEMOUT) aims to address this problem observing a sample of 35 high-mass star-forming cores at Galactocentric distances up to ~ 23 kpc with the Institut de RadioAstronomie Millimétrique (IRAM) 30m telescope in various 3mm and 2mm bands. In this work we analyse observations of methanol (CH_3OH), one of the simplest complex organic molecules crucial for organic chemistry in star-forming regions, and of two chemically related species, HCO and formaldehyde (H_2CO), towards 15 out of the 35 targets of the CHEMOUT sample. In fact, only targets previously detected in both HCO and H_2CO , which are precursors of CH_3OH , were considered.

Results. We detected CH_3OH in all 15 targets. The emission is associated with an extended envelope, as the average angular size is $\sim 47''$ (i.e. ~ 2.3 pc at a representative heliocentric distance of 10 kpc). Using a Local Thermodynamic Equilibrium approach, we derive CH_3OH excitation temperatures in the range $\sim 7 - 16$ K and line widths ≤ 4 km s⁻¹, consistent with emission from a cold and quiescent envelope. The CH_3OH fractional abundances w.r.t. H_2 range between $\sim 0.6 \times 10^{-9}$ and $\sim 7.4 \times 10^{-9}$. These values are comparable to those found in star-forming regions in the inner and local Galaxy. H_2CO and CH_3OH show well correlated line velocities, line widths, and fractional abundances w.r.t. H_2 , indicating that their emission is originated from similar gas. These correlations are not seen with HCO, suggesting that CH_3OH is likely more chemically related to H_2CO than to HCO.

Conclusions. Our results have important implications in the organic, and possibly pre-biotic, chemistry occurring in the outermost star-forming regions of the Galaxy, and can help setting the frontiers of the Galactic Habitable Zone.

Key words. Stars: formation – ISM: clouds – ISM: molecules

1. Introduction

The outer Galaxy (OG) is the portion of the Milky Way located beyond the Sun, that is at a distance from the Galactic Centre, R_{GC} , approximately in between the Solar circle (at ~ 8.34 kpc, Reid et al. 2014) and ~ 28 kpc (Digel et al. 1994). Inner and outer Galaxy show significantly different chemical properties. First, in the outer Galaxy the overall content of elements heavier than helium, defined as metallicity, is lower than the Solar one (e.g. Wenger et al. 2019). The elemental abundances of oxygen, carbon, and nitrogen, namely the three most abundant elements in the Universe after hydrogen and helium, decrease linearly (in logarithmic scale) as a function of R_{GC} (e.g. Esteban et al. 2017, Arellano-Córdova et al. 2020, Méndez-Delgado et al. 2022). Because of the lower abundances of heavy elements in the outer Galaxy with respect to the Solar ones and those of the inner Galaxy, it has been suggested that this zone is not suit-

able for forming planetary systems in which Earth-like planets could be born and might be capable of sustaining life (Prantzos 2008, Ramírez et al. 2010). The so-called Galactic Habitable Zone (GHZ) in the Milky Way is currently defined as an annular region about 2 kpc wide centred at R_{GC} 8 kpc, where the metallicity is appropriate to form Earth-like planets and where the occurrence of disruptive events such as supernovae is limited (Spitoni et al. 2014, 2017). Because of this, and also because of the fact that star-forming regions in the outer Galaxy are on average further away from us, the study of the formation of stars and planets, as well as the search for the basic bricks of life that could have favoured the emergence of life, were focused so far almost exclusively to the inner Galaxy, where the metallicity is Solar or super-Solar.

This scenario has been challenged by recent observational results. First, the occurrence of Earth-like planets does not seem to depend on the Galactocentric distance (e.g. Buchhave et al. 2012;

Table 1. Source list and parameters taken from paper I.

source	R.A. (J2000) h : m : s	Dec. (J2000) ° : ′ : ″	$N_{\text{CO}}(\text{H}_2)^{(a)}$ $\times 10^{21} \text{cm}^{-2}$	$N_{\text{Her}}(\text{H}_2)^{(b)}$ $\times 10^{22} \text{cm}^{-2}$	$\theta_c^{(c)}$ "	$R_{\text{GC}}^{(d)}$ kpc	$d^{(e)}$ kpc	rms ^(f) 3mm/2mm mK
WB89-379	01:06:59.9	65:20:51	6.5	5.76	14.6	16.4	10.2	7.5/13.5
WB89-380	01:07:50.9	65:21:22	11.4	–	–	16.0	9.7	7.7/12.1
WB89-391	01:19:27.1	65:45:44	5.2	–	–	16.1	9.7	6.6/11.1
WB89-399	01:45:39.4	64:16:00	6.3	4.06	34.1	16.0	9.4	6.2/9.7
WB89-437	02:43:29.0	62:57:08	14.2	–	–	15.7	8.6	7.7/13.7
WB89-501	03:52:27.6	57:48:34	11.2	–	–	15.6	8.0	7.8/14.8
WB89-621	05:17:13.4	39:22:15	13.0	14.5	11.7	18.9	10.6	9.1/14.8
WB89-789	06:17:24.3	14:54:37	5.8	13.7	12.4	19.1	11.0	6.8/12.0
19383+2711	19:40:22.1	27:18:33	–	–	–	13.2	14.8	6.4/9.3
19423+2541	19:44:23.2	25:48:40	–	20.1	8.3	13.5	15.3	8.1/10.2
WB89-006	20:42:58.2	47:35:35	6.3	–	–	14.3	12.2	4.7/6.7
WB89-035	21:05:19.7	49:15:59	5.2	6.2	11.9	13.1	10.1	5.7/11.0
WB89-076	21:24:29.0	53:45:35	5.0	5.6	10.5	15.1	11.8	7.8/11.6
WB89-080	21:26:29.1	53:44:11	8.5	2.8	18.1	12.8	8.9	7.4/12.6
WB89-283	23:32:23.8	63:33:18	5.8	2.8	10.5	15.8	10.4	4.6/6.9

(a) H_2 column density derived from CO (1–0) (Blair et al. 2008). The values are averaged within the Arizona Radio Observatory (ARO) main beam of $44''$;

(b) H_2 column density derived from Herschel measurements (Elia et al. 2021). The values are averaged within θ_c ;

(c) continuum angular size estimated from Herschel measurements (Elia et al. 2021);

(d) Galactocentric distance;

(e) heliocentric distance;

(f) 1σ rms achieved in the IRAM-30m spectra (Appendix-A) around the target CH_3OH lines.

Maliuk & Budaj 2020). This indicates that, even at metallicities lower than the Solar one, planets capable to host life can be found, depending also on the dynamical history of the planet host stars (Dai et al. 2021), which is likely to be different in the inner and outer Galaxy. Second, observations performed with the Atacama Large Millimeter Array (ALMA) towards the Large and Small Magellanic Clouds (LMC and SMC, Shimonishi et al. 2018, Sewiło et al. 2018, Sewiło et al. 2022), two external galaxies having metallicity ~ 3 and ~ 5 times lower than Solar, respectively, have detected emission of complex organic molecules (COMs), which are organic species with more than five atoms. This finding, and the recent discovery of a hot molecular core rich in COMs at R_{GC} of ~ 19 kpc (Shimonishi et al. 2021), have clearly suggested that the astrochemical processes that can lead to species of pre-biotic interest can be found also in metal poor environments. In particular, methanol (CH_3OH), one of the simplest but crucial COMs, was detected in star-forming regions associated with both the LMC and SMC, as well as with star-forming regions in the Milky Way up to $R_{\text{GC}} \sim 20$ kpc (Bernal et al. 2021). Methanol is thought to be a crucial species for pre-biotic chemistry as it is considered a possible parent species for larger organic molecules in both gas and ice (e.g. Charnley et al. 1992; Öberg et al. 2009; Chen et al. 2013; Chuang et al. 2016). Hence, its presence paves the way for the synthesis of more complex organic species.

In this paper we study the emission of methanol, of the formyl radical (HCO) and of formaldehyde (H_2CO) towards 15 high-mass star-forming regions in the OG with R_{GC} in between 13.1 and 19 kpc. Even though the OG is more extended than 19 kpc (see above), the R_{GC} range studied in this work is where the metallicity gradients are better constrained by observations (e.g. Esteban et al. 2017; Kovtyukh et al. 2022). Beyond 20 kpc, the metallicity gradients are much less well constrained (Spina et al. 2022). HCO and H_2CO are precursors of methanol (Watan-

abe & Kouchi 2002) and of other COMs relevant for pre-biotic chemistry such as formamide (e.g. Fedoseev et al. 2016), glycolaldehyde and ethylene glycol (Bennett & Kaiser 2007; Woods et al. 2012, 2013; Chuang et al. 2016, Rivilla et al. 2017, 2019). Hence, these observations can indicate us for the first time whether the formation pathways of CH_3OH , known to be efficient starting from Solar-like metallicities, are efficient also in the lower metallicity environment of the OG.

Our targets are part of CHEMOUT, an observational project described in Fontani et al. (2022, hereafter paper I) performed with the Institut de RadioAstronomie Millimétrique (IRAM) 30m telescope¹ that aims to study the chemical complexity in the low-metallicity environment of the OG. Sample and observations are described in Sect. 2. The data analysis is described in Sect. 3. The results are presented in Sect. 4 and discussed in Sect. 5.

2. Sample and observations

We targeted 15 sources extracted from the sample described in paper I. This sample is made of 35 targets selected from Blair et al. (2008), who searched for formaldehyde emission with the Arizona Radio Telescope (ARO) 12m telescope in dense molecular cloud cores in the OG. All cores are associated with IRAS colours typical of star-formation regions. The targets of this work, listed in Table 1, were selected because they were detected in both HCO (paper I) and H_2CO (Blair et al. 2008), and their R_{GC} cover a wide range among the sources detected in HCO (see paper I). In the same Table we give coordinates and other source parameters useful for the analysis, such as H_2 column densities estimated from previous works, and both Galactocentric and heliocentric (d) distances estimated in paper I.

¹ <http://www.iram.es/IRAMES/mainWiki/FrontPage>

Table 2. Parameters of the CH₃OH, HCO, and H₂CO transitions observed in this work and used in the analysis described in Sect. 3.

$\nu^{(1)}$ MHz	Quantum Numbers	$E_u^{(2)}$ K	$A_{ul}^{(3)}$ $\times 10^{-6} \text{ s}^{-1}$
CH ₃ OH			
3 mm			
96739.358	2(1,2)–1(1,1) E ₂	12.5	2.5
96741.371	2(0,2)–1(0,1) A ⁺	7.0	3.4
96744.545	2(0,2)–1(0,1) E ₁	20.1	3.4
96755.501	2(1,1)–1(1,1) E ₁	28.0	2.6
2 mm			
145093.707	3(0,3)–2(0,2) E ₁	27.1	12
145097.370	3(1,3)–2(1,2) E ₂	19.5	11
145103.152	3(0,3)–2(0,2) A ⁺	13.9	12
145124.410	3(2,2)–2(2,1) A ⁻	51.6	6.9
145126.191	3(2,1)–2(2,0) E ₁	36.2	6.8
145126.386	3(2,2)–2(2,1) E ₂	39.8	6.9
145131.855	3(1,2)–2(1,1) E ¹	35.0	11
145133.460	3(2,1)–2(2,0) A ⁺	51.6	6.9
HCO			
86670.760	$N_{K_a, K_b} = 1_{0,1} - 0_{0,0}, J = 3/2 - 1/2, F = 2 - 1$	4.2	4.7
86708.360	$N_{K_a, K_b} = 1_{0,1} - 0_{0,0}, J = 3/2 - 1/2, F = 1 - 0$	4.2	4.6
86777.460	$N_{K_a, K_b} = 1_{0,1} - 0_{0,0}, J = 1/2 - 1/2, F = 1 - 1$	4.2	4.6
86805.780	$N_{K_a, K_b} = 1_{0,1} - 0_{0,0}, J = 1/2 - 1/2, F = 0 - 1$	4.2	4.7
H ₂ CO			
140839.502	$J_{K_a, K_b} = 2_{1,2} - 1_{1,1}$	22	53
145602.949	$J_{K_a, K_b} = 2_{0,2} - 1_{0,1}$	10	78

⁽¹⁾ rest frequencies (ν); ⁽²⁾ energy of the upper level (E_u); ⁽³⁾ Einstein coefficient for spontaneous emission (A_{ul}).

The observed lines are listed in Table 2. All parameters of the CH₃OH and H₂CO lines are taken from the Cologne Database for Molecular Spectroscopy (CDMS², Endres et al. 2016), while for the HCO lines they are taken from the Jet Propulsion Laboratory (JPL³, Pickett et al. 1998).

Observations of the CH₃OH and H₂CO lines listed in Table 2 were performed with the IRAM-30m telescope in two observing runs (July and Septembre, 2021; project 042-21). We used the 3 and 2 mm receivers simultaneously. We note that 11 of our 15 targets were recently observed in the same CH₃OH lines at 3 mm by Bernal et al. (2021) with the ARO telescope, and 10 of them were detected. In this work, we reobserve these lines with higher sensitivity (rms of $\sim 5 - 10$ mK versus $\sim 17 - 200$ mK, in main beam temperature units) and higher angular resolution ($25''$ versus $63''$). Moreover, we add to the analysis the 2 mm lines, which have energies of the upper level up to ~ 50 K, and hence allow us to constrain the CH₃OH parameters, in particular T_{ex} , more accurately than with the 3 mm lines only, for which the range of energy of the upper level is $\sim 7 - 28$ K (Table 2). Sources WB89-006, WB89-789, WB89-035, and WB89-080 have been observed in both bands for the first time.

The Local Standard of Rest (LSR) velocities used to centre the spectra are listed in Table 1 of paper I. The observations were made in wobbler-switching mode with a wobbler throw of $220''$. Pointing was checked (almost) every hour on nearby quasars or bright HII regions. Focus was checked on planet Saturn at the start of observations and after sunset. The data were calibrated with the chopper wheel technique (see Kutner & Ulich 1981), with a calibration uncertainty of about 10%. The telescope half power beam width (HPBW) is $\sim 25''$ and $\sim 17''$ in the 3 and 2 mm bands, respectively. The spectra were obtained in main beam temperature units with the fast Fourier transform spectrom-

eter with channel width 200 kHz (FTS200), providing a spectral resolution of $\sim 0.6 \text{ km s}^{-1}$ and $\sim 0.4 \text{ km s}^{-1}$ at 3 and 2 mm, respectively. The total bandwidth observed is 90400 – 98180 MHz and 140720 – 148500 MHz at 3 and 2 mm, respectively. The 1σ rms noise level for each spectrum around the CH₃OH lines is given in Table 1.

The observations of the HCO lines listed in Table 2 were performed with the IRAM-30m telescope in the observing runs described in paper I. We refer to that paper for any observational and technical details related to these data.

3. Data reduction and analysis

The first steps of the data reduction (e.g. average of the scans, baseline removal, flag of bad scans and channels) were made with the CLASS package of the GILDAS⁴ software using standard procedures. Then, the baseline-subtracted spectra in main beam temperature (T_{MB}) units were fitted with the MAdrid Data CUBE Analysis (MADCUBA⁵, Martín et al. 2019) software.

The transitions of HCO, H₂CO, and CH₃OH in the bands described in Sect. 2 were identified via the SLIM (Spectral Line Identification and LTE Modelling) tool of MADCUBA. The lines were fitted with the AUTOFIT function of SLIM. This function produces the synthetic spectrum that best matches the data assuming a constant excitation temperature (T_{ex}) for all transitions. The other input parameters are: total molecular column density (N_{tot}), radial systemic velocity of the source (V), line full-width at half-maximum (FWHM), and angular size of the emission (θ_S). AUTOFIT assumes that V , FWHM and θ_S are the same for all transitions. These input parameters have all been left free except θ_S . In fact, θ_S can be computed for the CH₃OH and H₂CO lines observed also with the ARO-12m telescope by comparing the line intensities obtained with the two telescopes.

As said in Sect. 2, Bernal et al. (2021) detected the same 3 mm CH₃OH transitions in 10 of our 15 targets. Assuming that the brightness temperature distribution is Gaussian, as well as the beam of the two telescopes, and that there is no contamination from other sources when moving from the smaller to the larger beam, one finds that the angular size of the emission is given by (see also Eqs. (2) and (3) in Fontani et al. 2002):

$$\theta_S = \frac{\Theta_{\text{ARO}}^2 - \Theta_{\text{IRAM}}^2 (T_{\text{MB}}^{\text{IRAM}}/T_{\text{MB}}^{\text{ARO}})}{(T_{\text{MB}}^{\text{IRAM}}/T_{\text{MB}}^{\text{ARO}}) - 1}, \quad (1)$$

where Θ_{ARO} and Θ_{IRAM} are the half power beam widths of the two telescopes at the frequency of the observed lines, and $T_{\text{MB}}^{\text{ARO}}$ and $T_{\text{MB}}^{\text{IRAM}}$ are the main beam brightness temperature at line peak obtained with the ARO-12m and IRAM-30m telescope, respectively. We compare the intensity of the strongest transition, namely the 2(0,2)–1(0,1) A⁺ one at ~ 96741 MHz (Table 2). Θ_{ARO} and Θ_{IRAM} are $63''$ and $25''$, respectively, at ~ 97 GHz. For each source, $T_{\text{MB}}^{\text{IRAM}}$ was obtained by fitting the line with a single Gaussian in CLASS, and $T_{\text{MB}}^{\text{ARO}}$ was obtained by converting the line intensity given in Table 3 of Bernal et al. (2021) to T_{MB} units by dividing it by a factor 0.61. This conversion factor was taken from Appendix C.3 of the ARO-12m user manual⁶. $T_{\text{MB}}^{\text{ARO}}$, $T_{\text{MB}}^{\text{IRAM}}$, and the associated θ_S are reported in Table 3. For the sources for

⁴ <https://www.iram.fr/IRAMFR/GILDAS/>

⁵ MADCUBA is a software developed in the Madrid Center of Astrobiology (INTA-CSIC) which enables to visualise and analyse single spectra and data cubes: <https://cab.inta-csic.es/madcuba/>.

⁶ https://aro.as.arizona.edu/~aro/12m_docs/12m_userman.pdf

² <https://cdms.astro.uni-koeln.de/classic/>

³ <https://spec.jpl.nasa.gov/ftp/pub/catalog/catdir.html>

Table 3. CH₃OH line parameters.

source	$T_{\text{MB}}^{\text{ARO}}^{(1)}$ K	$T_{\text{MB}}^{\text{IRAM}}^{(1)}$ K	$\theta_{\text{S}}(\text{CH}_3\text{OH})^{(2)}$ arcsec	$V^{(3)}$ km s ⁻¹	$\text{FWHM}^{(3)}$ km s ⁻¹	$N_{\text{tot}}^{(3)}$ $\times 10^{13} \text{cm}^{-2}$	$T_{\text{ex}}^{(3)}$ K
WB89-379	0.04(0.01)	0.085	43(11)	-89.25(0.04)	1.65(0.10)	1.4(0.1)	11.0(1.0)
WB89-380	0.043(0.007)	0.102	42(8)	-86.48(0.05)	3.44(0.12)	3.5(0.2)	12.0(1.0)
WB89-391	0.06(0.008)	0.133	48(9)	-85.91(0.03)	1.48(0.08)	1.4(0.1)	10(1)
WB89-399	0.023(0.008)	0.029	110(35)	-82.21(0.06)	1.04(0.10)	0.25(0.05)	12(2)
WB89-437	0.09(0.01)	0.240	36(6)	-71.57(0.03)	2.98(0.08)	9.1(0.3)	14(0.5)
WB89-501	0.045(0.008)	0.094	51(11)	-58.63(0.05)	1.75(0.1)	1.5(0.1)	11.0(1.0)
WB89-621	0.20(0.01)	0.473	42(5)	-25.38(0.03)	1.74(0.06)	8.5(0.4)	12(1)
WB89-789	–	0.081	– ⁽⁴⁾	34.06(0.05)	2.10(0.13)	1.0(0.1)	9.7(0.8)
19383+2711	0.028	0.051	58(6)	-65.25(0.05)	2.17(0.12)	1.7(0.1)	15(1)
19423+2541	0.049(0.005)	0.111	45(7)	-72.42(0.05)	3.95(0.12)	4.1(0.1)	12.2(0.5)
WB89-006	–	0.108	– ⁽⁴⁾	-91.37(0.05)	2.92(0.12)	1.9(0.1)	9.6(0.5)
WB89-035	–	0.045	– ⁽⁴⁾	-77.70(0.07)	2.28(0.16)	1.1(0.8)	10.9(0.6)
WB89-076	0.087(0.008)	0.170	54(8)	-97.23(0.04)	1.56(0.10)	1.5(0.2)	7.0(0.5)
WB89-080	–	0.081	– ⁽⁴⁾	-74.41(0.06)	1.89(0.13)	1.0(0.1)	9.8(0.9)
WB89-283	–	0.058	– ⁽⁴⁾	-94.45(0.03)	1.31(0.07)	0.83(0.05)	16.4(1.4)

⁽¹⁾ peak intensity of the 2(0,2)–1(0,1) A⁺ transition observed with the ARO-12m ($T_{\text{MB}}^{\text{ARO}}$) and IRAM-30m ($T_{\text{MB}}^{\text{IRAM}}$) telescope, respectively. $T_{\text{MB}}^{\text{ARO}}$ was derived from the T_{a}^* units given in Bernal et al. (2021) as described in Sect. 3; on $T_{\text{MB}}^{\text{IRAM}}$, a calibration uncertainty of 10% is assumed;

⁽²⁾ angular size of the emission derived as explained in Sect. 3;

⁽³⁾ best fit parameters of the CH₃OH lines obtained with MADCUBA fixing the source size to the value in Col. 4: centroid velocity (V), full width at half maximum (FWHM), total column density (N_{tot}), and excitation temperature (T_{ex});

⁽⁴⁾ an average size of 47'' has been assumed to fit the data.

which the second strongest CH₃OH line is detected in both works, that is the 2(1,2)–1(1,1) E₂ transition at ~ 96739 MHz, we find angular sizes consistent within the uncertainties.

We performed the same analysis for the $J_{K_a, K_b} = 2_{1,2} - 1_{1,1}$ transition of H₂CO at ~ 140840 MHz, observed both in this work and in Blair et al. (2008). To convert the line intensities given in Table 1 of Blair et al. (2008) to T_{MB} units we divided their values by 0.87. Θ_{ARO} and Θ_{IRAM} are 44'' and 17'', respectively, at ~ 140 GHz. The obtained θ_{S} , and the intensities of the lines used to derive them, are listed in Table 4.

For both molecules, in all sources θ_{S} is larger (in some cases much larger) than the IRAM-30m beam. This indicates that the observed transitions trace an extended envelope of the cores. In fact, from the heliocentric distances given in Table 1, we derive that the linear size of the emitting region is ~ 1.5 – 5 pc for CH₃OH and ~ 0.9 – 6 pc for H₂CO. In Fig. 1, we plot the linear diameter, D , of H₂CO against that of CH₃OH, from which we see that $D[\text{CH}_3\text{OH}]$ and $D[\text{H}_2\text{CO}]$ are positively correlated. There are no systematic similarities or differences because $D[\text{CH}_3\text{OH}]$ is equal to $D[\text{H}_2\text{CO}]$ within the errors in three sources, larger in five, and smaller in two. Hence, this comparison indicates that the two tracers are associated with extended envelopes of comparable dimensions within a factor 2.

In the analysis performed with MADCUBA, for the five sources for which θ_{S} of CH₃OH could not be derived from the data, we have assumed the average angular size of the other sources (i.e. 47''). We have adopted this simplified approach because the five targets have similar heliocentric distances (in the range 8.9 – 12.2 kpc). However, we have checked how the results would change adopting for each source the angular size obtained from the average linear diameter computed from the sources with measured angular sizes, that is ~ 2.8 pc. Repeating the fits fixing θ_{S}

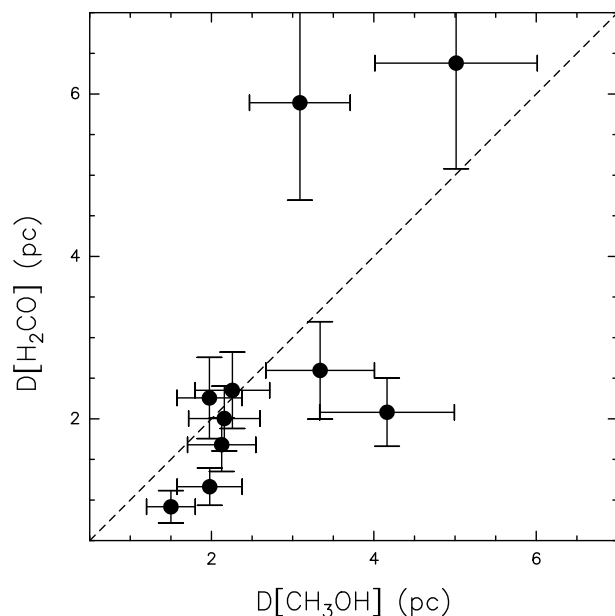


Fig. 1. Comparison between the linear diameters obtained for CH₃OH (x-axis) and H₂CO (y-axis) calculated from the angular diameters given in Tables 3 and 4, respectively, and the source heliocentric distances in Table 1. The dashed line is the locus where $D[\text{CH}_3\text{OH}] = D[\text{H}_2\text{CO}]$.

to these angular sizes, we obtain best fit results consistent within the uncertainties with the results obtained from the average angular size for both T_{ex} and N_{tot} . For HCO, because the size of the emission is unknown in the studied lines, we have assumed that the emission fills the telescope beam. The assumption is justified by the fact that the energies of the upper level of the observed transitions are very low (~ 4 K, Table 2), and that HCO is found

⁷ https://aro.as.arizona.edu/~aro/12m_docs/12m_userman.pdf

to trace the extended envelope of star-forming cores (e.g. Rivilla et al. 2019).

The best fit parameters obtained for CH₃OH are listed in Table 3. Those obtained for H₂CO and HCO are given in Table 4 and 5, respectively. For HCO, because the 4 observed lines have the same energies of the upper level, T_{ex} could not be derived from the data. Hence, we had to fix T_{ex} . We will discuss the assumed T_{ex} for HCO in Sect. 4.3.

4. Results

4.1. Methanol

We have detected CH₃OH emission in both observing bands towards all targets. The observed spectra and their best fits (superimposed on them) are shown in Figs. A.1 and A.2. The residuals, shown in Fig. A.3, are generally lower than, or comparable to, the 3σ rms noise (Table 1) towards all the methanol lines except for five targets that are WB89-391, WB89-437, WB89-621, WB89-006, and WB89-076, in which at least one CH₃OH line is significantly underestimated by the best fit. This cannot be due to (large) optical depth effects because the best fit opacities provided by MADCUBA are always below 0.1. However, considering that we assume a constant T_{ex} for all transitions, this can be due to marginal deviations from this simplified approach. As stated in Sect. 2, 11 out of our 15 targets were already observed in CH₃OH at 3 mm by Bernal et al. (2021) with the ARO telescope, and 10 of them were detected at 3 mm. In this work, we confirm all their detections and, thanks to our higher sensitivity, we confirm their tentative detection of CH₃OH claimed towards WB89-283. Moreover, we detect also the fainter 3 mm transitions at rest frequencies 96744.545 and 96755.501 MHz (Table 2), observed but undetected towards some targets in Bernal et al. (2021).

We find T_{ex} in the range 7 – 16.4 K, and FWHM of the lines in the range $\sim 1 - 4 \text{ km s}^{-1}$ (Table 1). These values confirm what already suggested by Bernal et al. (2021), and by the estimated angular sizes, namely that the emission is dominated by the cold and (relatively) quiescent gaseous envelope of the cores. This result is also in agreement with the low excitation energy of the transition from which θ_{S} is estimated ($E_{\text{u}} = 7 \text{ K}$, see Table 2). Bernal et al. (2021) also measured the kinetic temperatures from a non-LTE analysis, and derived values in the range 10–25 K. This would indicate that the methanol emission could be sub-thermally excited in several sources. It is not trivial to deduce if, and by how much, the methanol lines are sub-thermally excited, because the calculation of the critical densities of the CH₃OH lines is not straightforward. In fact, as discussed by Shirley (2015), the "typical" expression that includes only the Einstein coefficient for spontaneous emission and the collisional coefficient is valid only in a two-level approximation, not appropriate for molecules with spectrum as complex as that of methanol.

We have used RADEX on-line⁸ to test possible differences with respect to a non-LTE approach, especially for the sources for which our fitting procedure gives the highest residuals. For example, the intensity of the 3 mm lines in WB89-621 belonging to the $-A$ and $-E$ species can be reproduced assuming a kinetic temperature, T_{k} , of 15 K, line width equal to the observed one (1.74 km s^{-1} , Table 3), and a H₂ volume density, $n(\text{H}_2)$, of $3 \times 10^6 \text{ cm}^{-3}$. T_{k} and $n(\text{H}_2)$ are similar to the values obtained by Bernal et al. (2021) with their non-LTE approach. The resulting T_{ex} and total column density, N_{tot} , (derived as the sum of the column density of the $-A$ and $-E$ species) are 14 K and

$6 \times 10^{13} \text{ cm}^{-2}$, respectively, consistent with the estimates obtained with our approach ($T_{\text{ex}} \sim 12 \text{ K}$ and $N_{\text{tot}} \sim 8.5 \times 10^{13} \text{ cm}^{-2}$). The excitation temperatures and column densities are both comparable for the $-A$ and $-E$ species.

We note that a $n(\text{H}_2)$ of $\sim 10^6 \text{ cm}^{-3}$ could not be appropriate for the angular scales we are probing. In fact, from the H₂ column densities and diameters provided in Table 1 we derive for WB89-621 a $n(\text{H}_2)$ of $\sim 3 \times 10^3 \text{ cm}^{-3}$ when smoothed on the methanol source size of $42''$. We have then fixed in RADEX $n(\text{H}_2)$ to $\sim 3 \times 10^3 \text{ cm}^{-3}$, and again the FWHM to that observed and $T_{\text{k}} \sim 15 \text{ K}$. The line intensities can be reproduced with $N_{\text{tot}} \sim 1.3 \times 10^{14} \text{ cm}^{-2}$ ($7.2 \times 10^{13} \text{ cm}^{-2}$ for the $-A$ species, $6 \times 10^{13} \text{ cm}^{-2}$ for the $-E$ species), higher but still roughly consistent (within a factor 1.5) with the estimate found in the LTE approach also in this case. The excitation temperature is now $\sim 4 \text{ K}$, indicating sub-thermal excitation. However, even with different combinations of T_{k} , $n(\text{H}_2)$, and T_{ex} , N_{tot} must always be close to the value obtained in the LTE approach to reproduce the observed line intensities. Similar results can be obtained towards WB89-391, WB89-437, WB89-006, and WB89-076, for which a non-LTE approach considering $n(\text{H}_2)$ in the range $10^3 - 10^4 \text{ cm}^{-3}$ always needs values of N_{tot} consistent with the results obtained in LTE to reproduce the line intensities. In general, the non-LTE approach does not improve significantly the intensity ratios between $-A$ and $-E$ lines with respect to the LTE approach, except when using the unrealistic option of a different H₂ volume density for $-A$ and $-E$ species. Furthermore, the excitation temperatures for $-A$ and $-E$ species look consistent each other, and even assuming $-A$ and $-E$ ratios smaller than one does not improve the fit results significantly either.

This, and the general good agreement between the fits and the observed spectra (Figs. A.1, A.2, A.3), shows that our LTE analysis provides accurate total column densities, even if some transitions are likely sub-thermally excited.

Shimonishi et al. (2021) found that WB89-789, one of our targets, harbours a hot core in which the kinetic temperature measured with ALMA is higher than 100 K at scales $\leq 0.03 \text{ pc}$, obtained from CH₃OH lines. However, Shimonishi et al. (2021) estimated T_{ex} mostly from transitions with $E_{\text{u}} \geq 100 \text{ K}$, i.e. certainly arising from the inner hot core. We have produced with MADCUBA a synthetic spectrum fixing T_{ex} to 100 K, θ_{S} to $0.6''$ (corresponding to 0.03 pc at the source heliocentric distance of 11 kpc), and the column density to the value found by Shimonishi et al. (2021), i.e. $\sim 1.9 \times 10^{16} \text{ cm}^{-2}$. As expected, the resulting spectrum is within the noise level of our data, and hence does not give a significant/detectable contribution to the emission observed with the IRAM-30m telescope. This confirms that our observations trace only the external envelope of the hot core, and that in this and potentially also in the other targets higher angular resolution observations are needed to study the warmer more compact gaseous components.

The CH₃OH total column densities obtained towards our targets are in the range $\sim 0.25 \times 10^{13}$ and $\sim 8.5 \times 10^{13} \text{ cm}^{-2}$ (Table 3). These values are consistent within a factor ~ 2 with those estimated by Bernal et al. (2021) in the common targets, once a beam dilution factor to our values to match their beam of $63''$ is applied.

4.2. Formaldehyde

The two formaldehyde lines listed in Table 2, fitted and analysed as described in Sect. 3, are all clearly detected, as seen in the spectra of Figs. A.4 and A.5. The line at $\sim 140.8 \text{ GHz}$ was already detected in all sources by Blair et al. (2008) with an

⁸ <http://var.sron.nl/radex/radex.php>

Table 4. H₂CO line parameters.

source	$T_{\text{MB}}^{\text{ARO}(1)}$	$T_{\text{MB}}^{\text{IRAM}(1)}$	$\theta_{\text{S}}(\text{H}_2\text{CO})^{(2)}$	$V^{(3)}$	$\text{FWHM}^{(3)}$	$N_{\text{tot}}^{(3)}$	$T_{\text{ex}}^{(3)}$	$X_{\text{CO}}[\text{H}_2\text{CO}]^{(4)}$	$X_{\text{Her}}[\text{H}_2\text{CO}]^{(5)}$
	K	K	arcsec	km s ⁻¹	km s ⁻¹	$\times 10^{13}$ cm ⁻²	K	$\times 10^{-9}$ cm ⁻²	$\times 10^{-9}$ cm ⁻²
WB89-379	0.255	0.54	34(3)	-89.39(0.01)	1.75(0.04)	1.20(0.07)	31(2)	1.1(0.3)	1.2(0.3)
WB89-380	0.5713	0.93	48(5)	-86.65(0.04)	3.72(0.08)	3.8(0.3)	28(3)	4(1)	–
WB89-391	0.3463	0.55	50(5)	-86.03(0.02)	1.55(0.04)	0.85(0.06)	25(2)	2.1(0.6)	–
WB89-399	0.4425	0.48	140(14)	-82.16(0.02)	1.51(0.04)	0.6(0.2)	26(2)	10(2)	2.6(0.6)
WB89-437	0.57	1.80	22(2)	-71.42(0.02)	2.72(0.04)	9.3(0.5)	33(2)	1.6(0.4)	–
WB89-501	0.3075	0.73	30(3)	-58.46(0.02)	1.95(0.05)	2.1(0.2)	33(4)	0.9(0.3)	–
WB89-621	0.7863	1.50	39(4)	-25.33(0.03)	2.35(0.07)	4.0(0.1)	26(2)	2.4(0.5)	3.1(0.7)
WB89-789	0.2175	0.66	23(2)	34.20(0.03)	3.16(0.07)	3.2(0.8)	45(9)	1.5(0.7)	0.8(0.4)
19383+2711	0.2687	0.67	29(3)	-65.79(0.02)	2.60(0.06)	2.9(0.2)	36(5)	–	–
19423+2541	0.4813	1.00	35(4)	-72.59(0.02)	3.92(0.06)	6.5(0.6)	40(3)	–	6(2)
WB89-006	0.2037	0.33	49(5)	-91.29(0.07)	3.2(0.2)	1.1(0.1)	26(4)	2.2(0.7)	–
WB89-035	0.2188	0.45	36(4)	-77.58(0.02)	2.35(0.06)	1.4(0.1)	32(3)	1.8(0.5)	2.1(0.6)
WB89-076	0.3038	0.35	103(10)	-97.27(0.03)	1.84(0.06)	0.65(0.06)	28(3)	7(2)	11(3)
WB89-080	0.2387	0.53	33(3)	-74.47(0.03)	1.65(0.07)	1.1(0.2)	30(5)	0.7(0.3)	1.3(0.5)
WB89-283	0.2625	0.53	36(4)	-94.46(0.02)	1.56(0.04)	1.2(0.1)	35(5)	1.4(0.4)	5(2)

⁽¹⁾ peak intensity of the $J_{K_a, K_b} = 2_{1,2} - 1_{1,1}$ transition at ~ 140840 MHz observed with the ARO-12m ($T_{\text{MB}}^{\text{ARO}}$) and IRAM-30m ($T_{\text{MB}}^{\text{IRAM}}$) telescope, respectively. $T_{\text{MB}}^{\text{ARO}}$ was derived from the T_{r}^* units given in Blair et al. (2008) as described in Sect. 3. T_{r}^* is given without uncertainty in Blair et al. (2008). On $T_{\text{MB}}^{\text{IRAM}}$, a calibration uncertainty of 10% is assumed;

⁽²⁾ angular size of the emission derived as explained in Sect. 3;

⁽³⁾ best fit parameters of the CH₃OH lines obtained with MADCUBA fixing the source size to the value in Col. 4: centroid velocity (V), full width at half maximum (FWHM), total column density (N_{tot}), and excitation temperature (T_{ex});

⁽⁴⁾ fractional abundances w.r.t. H₂ computed from $N_{\text{CO}}(\text{H}_2)$, given in Table 1;

⁽⁵⁾ fractional abundances w.r.t. H₂ computed from $N_{\text{Her}}(\text{H}_2)$, given in Table 1.

angular resolution of 44". We confirm all their detections and add in the analysis the line at ~ 145.6 GHz. Some targets present hints of non-Gaussian high-velocity wings in the spectra of both transitions: WB89-437, WB89-621, 19423+2541, and WB89-080. All these sources were known to have high-velocity wings in the HCO⁺ $J = 1 - 0$ line (paper I). A second velocity feature towards 19383+2711, already found in HCO⁺, is clearly detected also in H₂CO. Two targets, WB89-380 and WB89-006, show hints of two peaks in the ~ 140.8 GHz line. In WB89-380, such profile is not seen in the other line at ~ 145.6 GHz, suggesting that it could be due to self-absorption. Instead, a similar profile is seen towards the other transition in WB89-006, suggesting that in this case a second velocity feature could also be responsible for the tentative second velocity peak. In all cases, however, the residuals of the Gaussian fits are low.

The best fit parameters are given in Table 4. The total column densities are in the range $0.6 - 9.3 \times 10^{13}$ cm⁻² similar to the CH₃OH ones. The excitation temperatures are in the range 25 – 45 K, i.e. significantly larger than those measured in CH₃OH (Table 3). We will discuss this result more accurately in Sect. 5.1.

4.3. Formyl radical

The four HCO transitions listed in Table 2 were fitted and analysed as described in Sect. 3. The observed spectra and the best fit superimposed on them are shown in Figs. A.6 and A.7. In most sources, three out of the four transitions are clearly detected at a significance level of $\sim 3\sigma$ rms or higher, while that at 86.80578 GHz, having the lowest line strength, is clearly detected only towards WB89-380 and WB89-391.

The best LTE fit parameters are given in Table 5. As said in Sect. 3, T_{ex} could not be derived from the observations because

the energies of the transitions were too close. Thus, as first order approach, we fixed T_{ex} to the values obtained from CH₃OH. We obtained FWHM in between 1.15 and 6.5 km s⁻¹, although the latter value, obtained towards 19383+2711, is very likely affected by the presence of a second unresolved velocity feature (clearly detected in HCO⁺ and c -C₃H₂, see paper I). Excluding this case, the measured FWHM are in between 1.15 and 3.3 km s⁻¹, similar to those measured in CH₃OH. The HCO total column densities are in the range $0.6 - 9.3 \times 10^{12}$ cm⁻², i.e. an order of magnitude lower than those of CH₃OH and H₂CO.

An alternative choice for T_{ex} would be that computed from H₂CO, which is likely closer to LTE conditions, as demonstrated by the good agreement between the LTE fits and the spectra (see Figs. A.4 and A.5). However, as we will discuss in Sect. 5.1, very likely HCO is associated with an envelope more extended and less turbulent than that traced by both H₂CO and CH₃OH, based on the significantly narrower line widths at half maximum. The excitation temperature of H₂CO thus likely represents the gas kinetic temperature of a region more turbulent (and likely more compact) than that traced by HCO. Therefore, the smaller T_{ex} derived from the (likely) sub-thermally excited CH₃OH lines could be closer to the real excitation conditions of HCO. In summary, it is not obvious to decide "a priori" which of the two T_{ex} is most appropriate, and thus we decided to fit the HCO lines also fixing T_{ex} to that of H₂CO. The results are given in Table B of Sect. B, and the alternative fits are shown in Figs. A.8 and A.9.

With respect to the results performed using the T_{ex} of CH₃OH (Table 5), line widths at half maximum and peak velocities are almost identical, while N_{tot} are systematically higher by a moderate factor (≤ 3) for all sources except for WB89-789 and 19423+2541, for which they are higher by a factor ~ 5.6 and ~ 3.8 , respectively. Because the alternative fits do not seem to

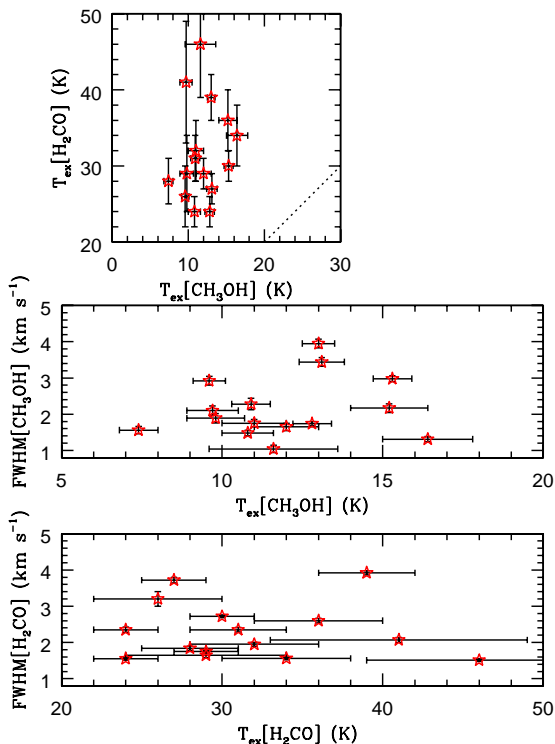


Fig. 2. *Top panel:* comparison between the best fit T_{ex} estimated from H_2CO and CH_3OH . The dotted line indicates $T_{\text{ex}}[\text{H}_2\text{CO}] = T_{\text{ex}}[\text{CH}_3\text{OH}]$. *Middle and bottom panels:* T_{ex} against FWHM measured from H_2CO (middle) and from CH_3OH (bottom). The CH_3OH and H_2CO parameters are given in Tables 3 and 4, respectively.

reproduce the observed spectra better than the first order ones (compare Figs. A.6 – A.7 with Figs. A.8 – A.9), it is not obvious to decide which approach is more accurate. In the following sections, we will consider the results derived from T_{ex} of CH_3OH , which we believe to better represent an envelope more extended than that traced by H_2CO , bearing in mind that they have to be considered as lower limits if the actual T_{ex} of HCO are higher.

5. Discussion

5.1. Excitation temperatures, FWHM and V of the lines

Inspection of Tables 3, 4 and 5 suggests that some molecular parameters obtained from CH_3OH , HCO, and H_2CO are similar, while others are significantly different. We examine first the best fit T_{ex} , FWHM and V .

The excitation temperatures measured from H_2CO are larger than those estimated from CH_3OH , and no correlation is found between the two T_{ex} estimates, as it can be seen from Fig. 2. We have also investigated whether the sources with higher T_{ex} , and hence potentially warmer (if T_{ex} is representative of T_{k}), are associated with gas emitting lines with larger FWHM, and hence more turbulent. As it can be noted from the middle and bottom panels in Fig. 2, we do not find any statistically significant correlation between T_{ex} and FWHM estimated both from H_2CO and CH_3OH . The different T_{ex} may be explained if CH_3OH traces gas colder than H_2CO . On the other hand, the best fit V for H_2CO and CH_3OH are very similar, as they differ by less than $\sim 0.2 \text{ km s}^{-1}$ in all targets (Fig. 3, top panel), and also the best fit FWHM are

very well correlated (Fig. 3, bottom panel). This, hence, suggests that the gas emitting H_2CO and CH_3OH could be made by layers, or portions, characterised by different (excitation) temperatures but belonging to a region kinematically and spatially coherent.

The best fit V derived for HCO and CH_3OH are different by up to $\sim 0.9 \text{ km s}^{-1}$, i.e. more than three times the difference in velocity between CH_3OH and H_2CO (Fig. 3, top panel). Even not including WB89-006, for which the difference is the largest ($\sim 0.9 \text{ km s}^{-1}$), still the range is $\sim 0.4 \text{ km s}^{-1}$, twice than that found for H_2CO and CH_3OH . Also, the lines FWHM derived for HCO do not appear correlated to those of CH_3OH , (Fig. 3, middle panel), indicating that the observed HCO emission could arise from material kinematically, and hence spatially, different from that responsible for the CH_3OH and H_2CO emission. In fact, as discussed also in Rivilla et al. (2019), HCO can be formed on dust grains through hydrogenation of iced CO (Tielens & Hagen 1982; Dartois et al. 1999; Watanabe & Kouchi 2002; Bacmann & Faure 2016), and in this case be the progenitor of H_2CO and CH_3OH , but also in the gas phase from atomic C and H_2O (Bacmann & Faure 2016; Hickson et al. 2016; Rivilla et al. 2019). In this case, the HCO emission should arise predominantly from an envelope in which C is still significantly in atomic form, likely more extended and diffuse than the region from where the emission of both H_2CO and CH_3OH arise, which requires most of C to be locked in CO and hence should be more dense.

Furthermore, as discussed in Pauly & Garrod (2018), even in iced HCO, hydrogenation of HCO will form either H_2CO or $\text{H}_2 + \text{CO}$ with equal probability, while, once formed, H_2CO is fairly robust and can quickly form CH_3O or CH_2OH , from which H addition to finally form CH_3OH is fast. For all these reasons, H_2CO and CH_3OH in cold environments are likely more related than HCO and CH_3OH , and our observational results are in agreement with this scenario. H_2CO can also form in the gas-phase (unlike CH_3OH) in regions where a significant fraction of C is not yet locked into CO. Our findings suggest that in these regions most of the C is indeed in form of CO, possibly because the present-day O/C ratio is larger than in the Sun neighbourhoods. We will discuss further this point in Sect. 5.4.

5.2. Fractional abundances of CH_3OH

From the $N_{\text{CO}}(\text{H}_2)$ listed in Table 1, we estimate the methanol fractional abundances with respect to H_2 , $X[\text{CH}_3\text{OH}]$. They are listed in Table 6 and are in the range $1.1\text{--}5.8 \times 10^{-9}$. These values are obtained by smoothing the column densities to the largest of the two angular sizes over which they are computed, which are θ_{S} for CH_3OH (Table 3), and $44''$ (i.e. the beam size) for $N_{\text{CO}}(\text{H}_2)$.

We have derived CH_3OH abundances also using $N(\text{H}_2)$ computed from Herschel Hi-GAL data, $N_{\text{Her}}(\text{H}_2)$, when available (Elia et al. 2021). The $N_{\text{Her}}(\text{H}_2)$ given in Hi-GAL, and computed from the spectral energy distribution of the sources, are averaged within the continuum angular sizes, θ_{c} , computed from the Herschel $250\mu\text{m}$ emission as explained in Elia et al. (2021). Both $N_{\text{Her}}(\text{H}_2)$ and θ_{c} are listed in Table 1, and the resulting $X[\text{CH}_3\text{OH}]$ is shown in Table 6. The two estimates of $X[\text{CH}_3\text{OH}]$ agree with each other within a factor 4, even though the computed range in this case is larger ($0.6\text{--}7.4 \times 10^{-9}$).

We have compared our results with star-forming regions at different metallicities: inner and local Galactic targets (representative of Solar and super-Solar metallicities), and OG cores and extragalactic sources (representative of sub-Solar metallicities). The list of these sources, with their abundances and reference works, is given in Table 6. Because we cannot constrain robustly the nature and evolutionary stage of our targets yet, we have

Table 5. HCO line parameters.

source	$V^{(1)}$ km s ⁻¹	FWHM ⁽¹⁾ km s ⁻¹	$N_{\text{tot}}^{(1)}$ $\times 10^{12}$ cm ⁻²	$T_{\text{ex}}^{(2)}$ K	$X_{\text{CO}}[\text{HCO}]^{(3)}$ $\times 10^{-10}$	$X_{\text{Her}}[\text{HCO}]^{(4)}$ $\times 10^{-10}$
WB89-379	-89.17(0.09)	2.6(0.2)	2.4(0.2)	11.0	3.7(0.6)	3.8(0.6)
WB89-380	-86.47(0.06)	3.3(0.1)	6.9(0.3)	12.0	6.1(0.8)	–
WB89-391	-85.94(0.04)	1.7(0.1)	3.0(0.1)	10.0	5.8(0.8)	–
WB89-399	-81.79(0.09)	2.0(0.2)	4.0(0.4)	12.0	6(1)	1.6(0.3)
WB89-437	-71.8(0.2)	2.8(0.4)	2.2(0.3)	14.0	1.6(0.4)	–
WB89-501	-58.32(0.07)	2.0(0.2)	3.1(0.2)	11.0	2.8(0.5)	–
WB89-621	-25.5(0.1)	2.0(0.2)	2.0(0.2)	12.0	1.5(0.3)	1.9(0.4)
WB89-789	34.21(0.08)	2.1(0.2)	3.2(0.3)	9.7	5(1)	2.9(0.5)
19383+2711	-68.6(0.2)	6.5(0.3)	9.3(0.4)	15.2	–	–
19423+2541	-72.53(0.09)	3.3(0.2)	5.0(0.3)	12.2	–	7(1)
WB89-006	-90.5(0.1)	1.4(0.3)	0.9(0.2)	9.6	1.4(0.4)	–
WB89-035	-77.61(0.07)	1.15(0.16)	1.3(0.2)	10.9	2.4(0.5)	2.8(0.6)
WB89-076	-97.1(0.1)	1.4(0.2)	0.6(0.1)	7.0	1.3(0.3)	2.0(0.5)
WB89-080	-74.0(0.1)	1.4(0.3)	1.4(0.3)	9.8	1.7(0.5)	3.0(0.8)
WB89-283	-94.4(0.14)	2.5(0.3)	2.5(0.3)	16.4	4(1)	16(4)

⁽¹⁾ Best fit parameters obtained with `MADCUBA`. We assumed that the emission fills the telescope beam;

⁽²⁾ fixed to the value obtained from CH_3OH (Table 1);

⁽³⁾ fractional abundance w.r.t. H_2 from $N_{\text{CO}}(\text{H}_2)$, given in Table 1;

⁽⁴⁾ fractional abundance w.r.t. H_2 from $N_{\text{Her}}(\text{H}_2)$, given in Table 1.

considered a large variety of star-forming regions, from early cold cores embedded in infra-red dark clouds (IRDCs), to protostellar objects and hot molecular cores in warmer and more evolved high-mass star-forming regions (HMSFs). Comparing our sources with targets located in the local and inner Galaxy (Table 6), we do not find significant or systematic differences. The clearest difference is seen towards the IRDC cores studied by Vasyunina et al. (2014): for these objects the CH_3OH abundances are on average higher than in our targets. However, our values overlap with the lower edge of their measured range. Moreover, the HMSF cores observed with angular resolutions similar to ours (e.g. Minier & Booth 2002, van der Tak et al. 2000, Gerner et al. 2014) show values overlapping with ours.

Comparing our results to those obtained in other low-metallicity environments, we find a very good agreement with the OG star-forming cores observed by Bernal et al. (2021), as expected since the two samples have several sources in common. Interestingly, the CH_3OH abundances measured in our study are lower than those measured towards the hot core embedded in WB89-789 (1.7×10^{-7}), as well as in the Small and large Magellanic Clouds ($\sim 10^{-8}$). This difference, however, is likely due to the higher excitation of the lines used to derive the abundances of the mentioned regions, having upper energies typically much larger than 100 K. These lines are associated with warmer (and likely more compact) gas, enriched in CH_3OH upon evaporation of dust grain mantles, than the one traced by the lines observed in this work, more likely associated with a colder envelope where a lot of CH_3OH is still frozen. In fact, Shimonishi et al. (2018) and Sewiło et al. (2018) claim that the CH_3OH emission arises from hot molecular cores embedded inside both the LMC and the SMC.

Of course, care needs to be taken in these comparisons, given the large number of important assumptions (e.g. the assumed gas-to-dust ratio to derive the $N(\text{H}_2)$ column density from the continuum, or the CO- H_2 conversion factor used to derive $N(\text{H}_2)$ from CO) that can influence significantly the abundance estimates

(see e.g. Nakanishi & Sofue 2006; Pineda et al. 2013). The probed linear scales are also, in several cases, very different.

5.3. Fractional abundances of HCO and H_2CO and their relation with CH_3OH

As for CH_3OH , we derived fractional abundances with respect to H_2 for H_2CO and HCO using both H_2 column density estimates given in Table 1. The results are listed in Tables 4 and 5, respectively. In Fig. 4 we compare the fractional abundances of methanol with those of HCO and H_2CO . For $X[\text{HCO}]$, we use the values derived assuming T_{ex} from CH_3OH , which are possibly more representative of an extended diffuse envelope (see Sect. 4.3), bearing in mind that the estimates using H_2CO are higher by a factor $\sim 1.5 - 3$. The plot indicates that $X[\text{HCO}]$ and $X[\text{CH}_3\text{OH}]$ are not correlated. We find a tentative positive correlation between $X[\text{H}_2\text{CO}]$ and $X[\text{CH}_3\text{OH}]$ (Pearson's ρ correlation coefficient ~ 0.3). This would support our previous claim (Sect. 5.1), based on the V and FWHM of the lines, that the CH_3OH emission is more likely related to H_2CO emission than to HCO emission. However, care needs to be taken in the interpretation of these plots since the correlation is tentative, it is strongly influenced by one single source, WB89-399, and H_2CO is also known to form in the gas phase (unlike CH_3OH) from regions rich in hydrocarbons, i.e. where C is not yet completely locked in CO (see e.g. Chacon-Tanarro et al. 2019).

5.4. Abundance variations with the Galactocentric distance

In Fig. 5 we show the CH_3OH , HCO, and H_2CO abundances against the source Galactocentric distances, R_{GC} . The filled symbols show the abundances calculated using $N_{\text{CO}}(\text{H}_2)$, while the empty ones illustrate those calculated using $N_{\text{Her}}(\text{H}_2)$ (Table 1). Again, for HCO we show the results obtained using as T_{ex} the excitation temperatures of CH_3OH , being more likely representative of an envelope more extended than that traced by H_2CO . A simple linear regression fit to the data (solid line) shows an almost

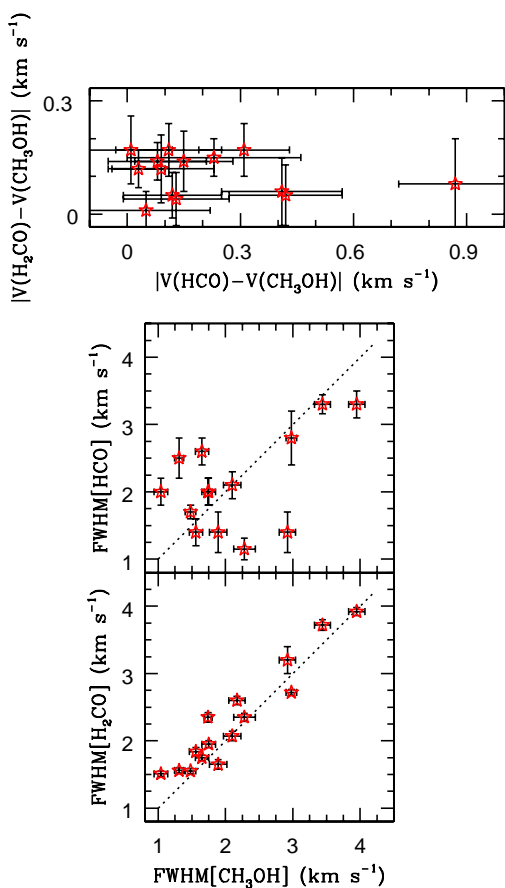


Fig. 3. *Top panel:* velocity difference between H_2CO and CH_3OH against that between HCO and CH_3OH . *Middle and bottom panels:* comparison between the FWHM measured for HCO and CH_3OH (middle) and that measured from CH_3OH and H_2CO (bottom). The dotted line indicates $\text{FWHM}[\text{HCO}] = \text{FWHM}[\text{CH}_3\text{OH}]$ or $\text{FWHM}[\text{H}_2\text{CO}] = \text{FWHM}[\text{CH}_3\text{OH}]$. In all panels, we have not included the HCO data for 19383+2711, for which the resulting fit parameters are affected by the unresolved second velocity feature (see Sect. 4.3).

flat line, indicating that all abundances seem independent of R_{GC} . This suggests that the decreasing metallicity towards the external part of the Galaxy should not have effect on the abundance of CH_3OH . This result was already found by Bernal et al. (2021). The main novelty of this study is that also for HCO and H_2CO , two progenitors of CH_3OH , the abundance does not decrease at metallicities lower than the Solar one.

However, both abundance estimates are based on crucial assumptions: in the method of Blair et al. (2008), a CO-H_2 conversion factor is assumed independent on R_{GC} , while departures from a constant value are both observed and expected in both the Milky Way and external galaxies (Bolatto et al. 2013; Pineda et al. 2013; Casasola et al. 2017; 2020); in the method of Elia et al. (2021), a constant gas-to-dust ratio of 100 is assumed, which is also expected to change radially (e.g. Magrini et al. 2011). For the former, a Galactocentric trend has been proposed by Nakanishi & Sofue (2006, see their Eq.(2)), from which the CO-H_2 conversion factor would vary by a factor ~ 2 from 13 to 19 kpc, still consistent with an almost flat trend of the molecular abundances with R_{GC} . For the latter, we have investigated how the abundances change considering the Galactocentric increasing trend found by Giannetti et al. (2017) for the gas-to-dust ratio. In Fig. 5, we plot the abundances of CH_3OH , HCO , and

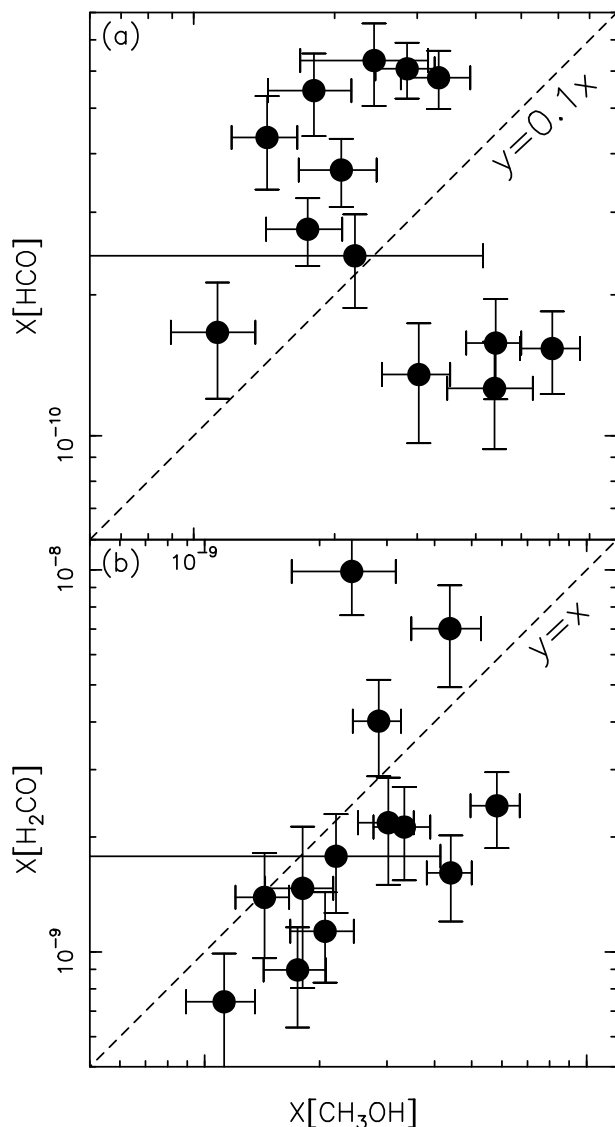


Fig. 4. (a): comparison between the HCO and CH_3OH fractional abundances derived from $N_{\text{CO}}(\text{H}_2)$. The dashed line indicates the locus where $y=0.1x$; (b): same as panel (a) for H_2CO and CH_3OH . The dashed line indicates the locus where $y=x$.

H_2CO derived from $N_{\text{Her}}(\text{H}_2)$ corrected according to Eq. (2) in Giannetti et al. (2017):

$$\text{Log}(\gamma) = (0.087 \pm 0.007) \times R_{\text{GC}} + (1.44 \pm 0.03), \quad (2)$$

where γ is the gas-to-dust ratio. We do not include the systematic uncertainties for simplicity. Please note that Eq. (2) assumes the same Solar Galactocentric radius as we do.

As expected, now all molecules show abundances decreasing with R_{GC} . However, this overall decrease does not seem to imply a reduced efficiency in the formation of these organics, as we will discuss in the following sub-sections.

5.4.1. CH_3OH

Let us start examining the case of CH_3OH . A linear regression fit applied to the points plotted in panel (a) of Fig. 5 gives:

$$X[\text{CH}_3\text{OH}] = (-1.14 \times 10^{-10}) \times R_{\text{GC}} + 2.45 \times 10^{-9}, \quad (3)$$

which implies that $X[\text{CH}_3\text{OH}]$ decreases by a factor ~ 5 from 8.34 kpc (the Sun's Galactocentric distance) to 19 kpc, extrapolating the trend found in the OG to the local Galaxy. According to the gradients given in Arellano-Córdova et al. (2020), the $[\text{O}/\text{H}]$ and $[\text{C}/\text{H}]$ ratios at 19 kpc are $\sim 1.2 \times 10^{-4}$ and $\sim 4.7 \times 10^{-5}$, i.e. ~ 3 and ~ 6 times lower, respectively, than the values at the Solar circle ($[\text{O}/\text{H}] \sim 3 \times 10^{-4}$ and $[\text{C}/\text{H}] \sim 2.8 \times 10^{-4}$). The more recent gradients given in Méndez-Delgado et al. (2022) provide $[\text{O}/\text{H}] \sim 1.1 \times 10^{-4}$ and $[\text{C}/\text{H}] \sim 3.9 \times 10^{-5}$, respectively, at 19 kpc, i.e. ~ 3 and ~ 7 times lower than Solar ($[\text{O}/\text{H}] \sim 3.1 \times 10^{-4}$ and $[\text{C}/\text{H}] \sim 2.6 \times 10^{-4}$).

Therefore, the observed scaling factor of $X[\text{CH}_3\text{OH}]$ when applying the gas-to-dust ratio correction is consistent with that of the $[\text{C}/\text{H}]$ ratio, or even marginally smaller than it. This suggests that the "efficiency" in the formation of CH_3OH , scaling with the availability of the parent element C, is at least as high as in the local Galaxy.

5.4.2. HCO and H_2CO

Similarly, for $X[\text{HCO}]$ and $X[\text{H}_2\text{CO}]$ we find a negligible decrease with R_{GC} without considering the Galactocentric variation of the gas-to-dust ratio, and a decrease similar to that of CH_3OH when applying it. In fact, the linear regression fits to the points plotted in Fig. 5 provide:

$$X[\text{HCO}] = (-1.38 \times 10^{-11}) \times R_{\text{GC}} + 2.95 \times 10^{-10}; \quad (4)$$

$$X[\text{H}_2\text{CO}] = (-1.18 \times 10^{-10}) \times R_{\text{GC}} + 2.51 \times 10^{-9}. \quad (5)$$

These relations imply that both $X[\text{HCO}]$ and $X[\text{H}_2\text{CO}]$ decrease by a factor ~ 5.5 from 8.34 kpc to 19 kpc. However, several caveats must be taken into consideration. First, the Galactocentric trend for the gas-to-dust ratio is associated with large systematic and statistical uncertainties (Giannetti et al. 2017), and local values may deviate significantly from the proposed trend. Second, our linear regression fit is obtained in the range $R_{\text{GC}} \sim 13$ –19 kpc and could not be appropriate down to $R_{\text{GC}} \sim 8.34$ kpc. Third, the comparison with Galactocentric gradients needs to be taken with caution because the elemental abundances are still under debate. For example, the already mentioned $[\text{C}/\text{H}]$ decrease by a factor 6 from the Solar circle to 19 kpc found by Arellano-Córdova et al. (2020) is consistent with the 5.5 scaling factor predicted by Eqs. (4) and (5). However, the more recent gradients derived by Méndez-Delgado et al. (2022) indicate a scaling factor of ~ 7 for $[\text{C}/\text{H}]$, that is marginally higher than our estimates.

Therefore, notwithstanding the above mentioned uncertainties, one can conclude that the formation of these molecules is not inhibited in low-metallicity regimes, because all of them show abundances that are in line with the initial local abundances of the parent elements, and very likely not smaller than them. As discussed in Blair et al. (2008), Bernal et al. (2021), and in paper I, this finding, and the additional evidence that Earth-like planets are ubiquitously found in the Galaxy (Sect. 1), suggest that an appropriate "ground" for the formation of habitable planets is present also in the OG, and calls for a redefinition of the GHZ that takes requirements other than metallicity into account.

5.4.3. Abundance ratios

Finally, the column density ratios $N[\text{CH}_3\text{OH}]/N[\text{HCO}]$ as a function of R_{GC} are shown in the bottom panel of Fig. 5, and range from ~ 3 (19383+2711) to ~ 38 (WB89-621), with an average

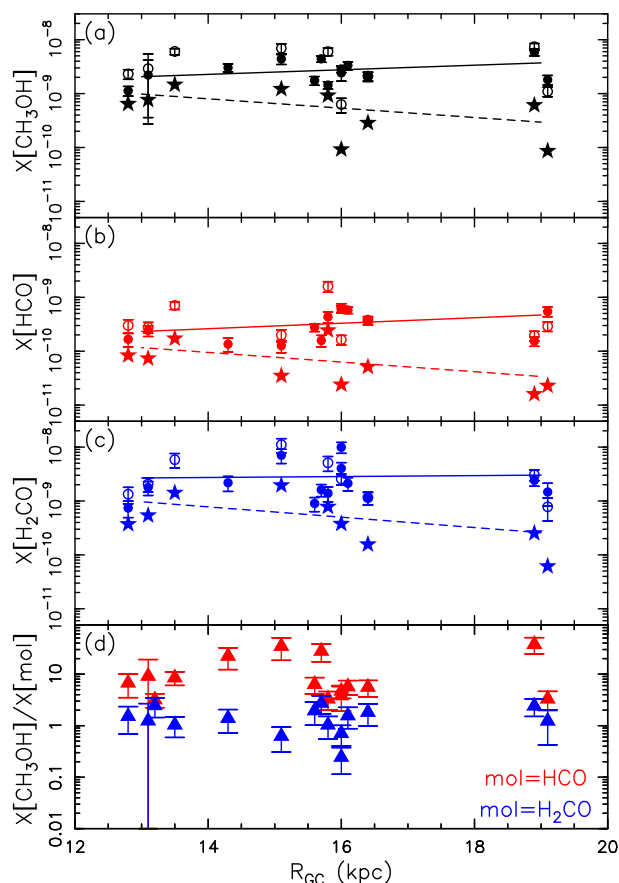


Fig. 5. Panels (a), (b) and (c): fractional abundances of, from top to bottom, CH_3OH , HCO , and H_2CO , as a function of R_{GC} . The fractional abundances are derived from $N_{\text{CO}}(\text{H}_2)$ given in Blair et al. (2008) (filled circles, Table 1) and from $N_{\text{Her}}(\text{H}_2)$ given in Elia et al. (2021) (empty circles, Table 6). The stars correspond to the values computed from $N_{\text{Her}}(\text{H}_2)$ corrected for the Galactocentric trend for the gas-to-dust ratio given in Giannetti et al. (2017). In all panels, the solid and dashed lines connect the values obtained at 13 and 19 kpc from a linear regression fit applied to the points computed from $N_{\text{Her}}(\text{H}_2)$ without and with corrections, respectively, for the Galactocentric trend of the gas-to-dust ratio.

Panel (d): abundance ratios $X[\text{CH}_3\text{OH}]/X[\text{HCO}]$ (red triangles) and $X[\text{CH}_3\text{OH}]/X[\text{H}_2\text{CO}]$ (blue triangles) as a function of R_{GC} .

value of ~ 12 (median ~ 6.4). The ratios $N[\text{CH}_3\text{OH}]/N[\text{H}_2\text{CO}]$, shown in the same plot are in between ~ 0.2 (WB89-399) and ~ 2.7 (WB89-437), with an average value of ~ 1.5 (median 1.4). The latter values are consistent with those measured by Bernal et al. (2021). Both ratios do not change with R_{GC} , indicating once more that the chemistry that connects these species do not seem to vary (at least in an obvious way) with the distance from the Galactic Centre.

5.5. Methanol formation at low metallicity

The formation of CH_3OH in dense star-forming cores is usually attributed to be mostly due to hydrogenation of CO which, on the surfaces of dust grains, forms sequentially HCO , H_2CO , CH_2OH , and finally CH_3OH . This is largely believed to be the most important formation route, given the inefficiency of gas phase routes at low temperatures (e.g. Garrod et al. 2006). If the main formation route is the same in the low metallicity environment of the OG, the large abundances measured in this study would suggest an active surface chemistry, followed by desorption mechanisms. In

this respect, mantle evaporation either from internal protostellar activity, or from external processes, are typically invoked. Reactive desorption can also be important. As described by Vasyunin et al. (2017), reactive desorption becomes very efficient in regions where icy mantles become CO-rich (i.e. in dense gas where the catastrophic CO freeze-out takes place and CO ice becomes the dominant component of the icy mantles). In paper I, we have reported the detection of SiO $J = 2 - 1$ in 46% of the 35 targets. Among the 15 sources studied in this paper, 10 are clearly or tentatively associated with SiO emission, while five (WB89-789, WB89-006, WB89-076, WB89-080, and WB89-283) are not. On the other hand, all sources but 19383+2711 are associated with high-velocity wings in the HCO⁺ $J = 1 - 0$ line (paper I). This suggests that, even in the OG, the origin of CH₃OH emission could be connected to evaporation of grain mantles caused by protostellar outflows. The non detection of SiO in the five targets mentioned above may be due to insufficient sensitivity, given that these objects are not the most intense of the sample in the molecular lines analysed both in this paper (see Figs. A.1 – A.5) and in paper I. However, first, the methanol line widths for all sources are narrow with respect to what is expected from material freshly released from outflows. Second, the full analysis of both SiO and HCO⁺ lines goes beyond the scope of this work and will be performed in a forthcoming paper (Fontani et al. in prep.). Moreover, this result could also be influenced by the source selection we have performed in this study, and should be corroborated with a higher statistics.

Chemical models with modified (lower) metallicities were developed in the past to interpret the formation of methanol and other COMs in the Magellanic Clouds as representatives of low-metallicity environments. Acharyya & Herbst (2015) modelled dense and cold clouds of the LMC. They found that some observed results, especially for methanol, are better matched if these regions currently have lower temperatures. This is in agreement with the low temperature associated with our observed methanol emission. Moreover, Acharyya & Herbst (2016) modelled dense clouds of the SMC, in which the metallicity is lower than the Solar one by a factor 5, and found that for species produced fully (e.g., CH₃OH) or partially on the grain surfaces (e.g., H₂CO), the predicted abundances are not just metallicity-scaled values but they change in a more complex way. Our observations also indicate that care needs to be taken in the comparison with scaled-metallicity values, because different assumptions in the derivation of the abundances can bring to different conclusions (see Sect. 5.4).

Pauly & Garrod (2018) used the gas-grain chemical model MAGICKAL to model the chemistry in clouds of the Magellanic clouds where massive young stellar objects are forming. They discuss the formation and evolution of several species chemically connected to CH₃OH, and of CH₃OH itself, and conclude that the methanol abundance is even found to be enhanced in low-metallicity environments. In fact, their models predict that the amount of CH₃OH with respect to CO increases as the elemental C decreases, thus indicating a more efficient abundance at lower metallicities. This effect could be due to the smaller C/O ratio (see Sect. 5.4), so that the bulk of C is in the form of CO, required to form CH₃OH. If confirmed, this would imply a lower abundance of carbon-chains, or other carbon rich molecules. The exploitation of the detected carbon-rich species, listed in paper I, among which *c*-C₃H₂, C₄H, and CCS, will be performed in forthcoming papers (Fontani et al., in prep.).

However, when modelling the chemistry, several ingredients need to be considered and many crucial ones could vary significantly with the Galactocentric radius. For example, as also dis-

cussed, e.g., in Viti et al. (2020), the abundances of molecules containing carbon in external galaxies known to be associated with different visual extinctions, cosmic-ray ionisation rates, and/or Ultraviolet (UV) radiation fields are predicted to change by orders of magnitude. Because the parameters aforementioned are expected to vary within the Milky Way as well (e.g. both the interstellar UV field and the cosmic-ray ionisation rate are expected to be lower in the OG due to less numerous of massive stars and of supernovae explosions), to appropriately model the chemistry a thorough analysis of the variations with R_{GC} of all these key parameters is absolutely needed. This discussion is particularly urgent, since important complex species in external galaxies are now detected easily thanks to the available powerful (sub-)mm telescopes (see e.g. the first results of the ALCHEMI ALMA large program, Martín et al. 2021), showing that a rich chemistry can develop even in external galaxies. This goes beyond the scope of this paper, but strongly calls for both observational works to measure and constrain these parameters as a function of the Galactic radius, and theoretical works aimed at identifying the physical conditions that mostly affect the chemistry in such modified environments. In particular, chemical evolution models (e.g. Romano et al. 2020) could be used in the future to estimate the amount and density of massive stars, important sources of both UV photons and cosmic rays, as a function of the Galactocentric radius.

6. Conclusions

We detected CH₃OH, HCO, and H₂CO emission associated with 15 star-forming regions of the outer Galaxy. Derived angular diameters, excitation temperatures and line widths of CH₃OH indicate that the emission is dominated by a cold and quiescent gaseous envelope. The CH₃OH fractional abundances are in the range $\sim 0.6 - 7.4 \times 10^{-9}$. These values are consistent with similar star-forming regions in the local and inner Galaxy. We find that some CH₃OH line parameters, such as centroid velocity, FWHM, and (less obviously) fractional abundance with respect to H₂, are correlated to those of H₂CO, while they do not appear correlated to those of HCO. This may indicate that hydrogenation of CH₃OH from iced H₂CO, followed by evaporation or other desorption mechanisms from grain mantles, can be the relevant source of CH₃OH also in the OG. On the other hand, the HCO emission we observe can also be significantly produced in the gas phase from routes not involving H₂CO and CH₃OH. However, in these observations the CH₃OH emission is clearly associated with an extended and relatively quiescent envelope rather than with shocked or sputtered material, hence this conclusion needs to be corroborated by higher-angular resolution observations. The total column densities and fractional abundances with respect to H₂ indicate that the production of CH₃OH is not inhibited even at Galactocentric distances of ~ 19 kpc, where the carbon abundance is estimated to be lower by a factor $\sim 6 - 7$ with respect to the Solar one. In fact, even considering corrections to the estimated abundances taking the variations of the gas-to-dust ratio with R_{GC} into account, our abundances are in line with metallicity-scaled values. The high abundance of CH₃OH at large R_{GC} could be due to the smaller C/O ratio at these large Galactocentric distances, that implies that the bulk of C is in the form of CO, required to form CH₃OH. Our results confirm that organic chemistry is active and efficient even in the outermost star-forming regions of the Milky Way, and support the idea that the outer boundaries of the Galactic Habitable Zone need to be re-discussed in light of the capacity of the interstellar medium to form organic molecules even at such low metallicities.

Table 6. Abundances of CH₃OH calculated in this work, and towards other star-forming regions in the Galaxy, as well as in external galaxies.

	$X_{\text{CO}}[\text{CH}_3\text{OH}]^{(a)}$ $\times 10^{-9}$	$X_{\text{Her}}[\text{CH}_3\text{OH}]^{(b)}$ $\times 10^{-9}$
WB89-379	2.1(0.4)	2.1(0.4)
WB89-380	2.9(0.4)	–
WB89-391	3.3(0.6)	–
WB89-399	2.4(0.7)	0.6(0.2)
WB89-437	4.4(0.6)	–
WB89-501	1.8(0.3)	–
WB89-621	5.8(0.9)	7.4(1.1)
WB89-789	1.8(0.4)	1.1(0.2)
19383+2711	–	–
19423+2541	–	6.0(0.7)
WB89-006	3.0(0.5)	–
WB89-035	2.2(1.3)	2.9(2.5)
WB89-076	4.4(0.9)	6.9(1.4)
WB89-080	1.1(0.2)	2.3(0.5)
WB89-283	1.4(0.2)	6.0(1.0)
Inner and local Galaxy	$X[\text{CH}_3\text{OH}]$	Ref. ^(c)
IRDC cores	$0.52\text{--}65 \times 10^{-9}$	(1)
IRDC cores	$\leq 1 \times 10^{-9}$	(2)
HMSF cores	$0.07\text{--}1.5 \times 10^{-9}$	(3)
HMSF cores	0.9×10^{-9}	(2)
Hot cores	2.6×10^{-8}	(2)
HMSF cores	$0.4\text{--}24 \times 10^{-9}$	(4)
OG cores and low-metallicity galaxies		
OG cores	$0.2\text{--}4.9 \times 10^{-9}$	(5)
WB89-789 hot core	1.7×10^{-7}	(6)
Small Magellanic Cloud	$0.5\text{--}1.5 \times 10^{-8}$	(7)
Large Magellanic Cloud	$2 \times 10^{-10}\text{--}5.6 \times 10^{-8}$	(8, 9)

^(a) from $N_{\text{CO}}(\text{H}_2)$, given in Table 1;^(b) from $N_{\text{Her}}(\text{H}_2)$, given in Table 1;^(c) References: (1) Vasyunina et al. (2014, averaged on an angular scale of 29''); (2) Gerner et al. (2014, averaged on an angular scale of 11''); (3) Minier & Booth (2002, averaged on an angular scale of 34''); (4) van der Tak et al. (2000, averaged on an angular scale of 18''); (5) Bernal et al. (2021), averaged on a beam of 63''); (6) Shimonishi et al. (2021, averaged on an angular scale of 1.9''); (7) Shimonishi et al. (2018, averaged on an angular scale of $\sim 0.6''$); (8) Sewiło et al. (2018, averaged on an angular scale of $\sim 0.8''$); Sewiło et al. (2022, averaged on an angular scale of $\sim 0.8''$).

Acknowledgements. We thank the anonymous Referee for their valuable and constructive comments. F.F. is grateful to the IRAM 30m staff for their precious help during the observations. L.C. has received partial support from the Spanish State Research Agency (AEI; project number PID2019-105552RB-C41). V.M.R. acknowledges support from the Comunidad de Madrid through the Atracción de Talento Investigador Modalidad I (Doctores con experiencia) Grant (COOL: Cosmic Origins of Life; 2019-T1/TIC-15379). This publication was supported by the European Union Horizon 2020 research and innovation programme under grant agreement No 730562 and grant agreement No 101004719 [ORP] (RadioNet).

References

Acharyya, K. & Herbst, E. 2015, ApJ, 812, 142A

Acharyya, K. & Herbst, E. 2016, ApJ, 822, 105A

Arellano-Córdova, K.Z., Esteban, C., García-Rojas, J., Méndez-Delgado, J.E. 2020, MNRAS, 496, 1051

Bacmann A., Faure A., 2016, A&A, 587, A130

Bennett C.J. & Kaiser R.I., 2007, ApJ, 661, 899

Bernal, J.J., Sefhus, C.D., Ziurys, L.M. 2021, ApJ, 922, 106

Blair, S.K., Magnani, L., Brand, J., Wouterloot, J.G.A. 2008, AsBio, 8, 59

Bolato, A.D., Wolfire, M., Leroy, A.K. 2013, ARA&A, 51, 207

Buchhave, L.A., Latham, D.W., Johansen, A., Bizzarro, M., Torres, G., et al. 2012, Nature, 486, 375

Casasola, V., Cassarà, L.P., Bianchi, S., Verstocken, S., Xilouris, E., et al. 2017, A&A, 605, 18

Casasola, V., Bianchi, S., De Vis, P., Magrini, L., Corbelli, E., et al. 2020, A&A, 633, 100

Chacon-Tanarro, A., Caselli, P., Bizzocchi, L., Pineda, J.E., Sipilä, O., et al. 2019, A&A, 622, 141

Charnley, S.B., Tielens, A.G.G.M. & Millar, T.J. 1992 ApJL, 399, L71

Chen, Y.-J., Ciaravella, A., Muñoz Caro, G.M., et al. 2013 ApJ, 778, 162

Chuang K.-J., Fedoseev G., Qasim D., Ioppolo S., van Dishoeck E.F., Linnartz H. 2016, MNRAS, 467, 2552

Dai, Y.-Z., Liu, H.-G., An, D.-S., Zhou, J.-L. 2021, AJ, 162, 46

Dartois E., Demyk K., d'Hendecourt L., Ehrenfreund P., 1999, A&A, 351, 1066

Digel, S., de Geus, E., Thaddeus, P. 1994, ApJ, 422, 92

Elia, D., Merello, M., Molinari, S., et al. 2021, MNRAS, 504, 2742

Endres, P., Schlemmer, S., Schilke, P., Stutzki, J., Müller, H.S.P. 2016, J.Mol.Spec., 327, 95

Esteban, C., Fang, X., García-Rojas, J., Toribio San Cipriano, L. 2017, MNRAS, 471, 987

Fedoseev G., Chuang K.-J., van Dishoeck E.F., Ioppolo S., Linnartz H. 2016, MNRAS, 460, 4297

Fontani, F., Cesaroni, R., Caselli, P., Olmi, L. 2002, A&A, 389, 603

Fontani, F., Colzi, L., Bizzocchi, L., Rivilla, V.M., Elia, D. et al. 2022,

Garrod, R., Park, I.H., Caselli, P., Herbst, E. 2006, FaDi, 133 51

Gerner, T., Beuther, H., Semenov, D., Linz, H., Vasyunina, T., Bihr, S., Shirley, Y. L., Henning, Th. 2014, A&A, 563, 97

Giannetti, A., Leurini, S., König, S., et al. 2017, A&A, 606, L12

Hickson K. M., Loison J.-C., Nunez-Reyes D., Mereau R., 2016, preprint, (arXiv:1608.08877)

Kovtyukh, V., Lemasle, B., Bono, G., Usenko, I. A., da Silva, R., et al. 2022, MNRAS, 510, 1894

Kutner, M.L., & Ulich, B.L. 1981, ApJ, 250, 341

Magrini, L., Bianchi, S., Corbelli, E., Cortese, L., Hunt, L., et al. 2011, A&A, 535, 13

Maliuk, A. & Budaj, J. 2020, A&A, 635, 191

Martín, S., Martín-Pintado, J., Blanco-Sánchez, C., Rivilla, V.M., Rodríguez-Franco, A., Rico-Villas, F. 2019, A&A, 631, 159

Martín, S., Mangum, J.G., Harada, N., Costagliola, F., Sakamoto, K., et al. 2021, A&A, 656, 46

Méndez-Delgado, J.E., Amayo, A., Arellano-Córdova, K.Z., Esteban, C., García-Rojas, J., Carigi, L., Delgado-Inglada, G. 2022, MNRAS, 510, 4436

Minier, V. & Booth, R.S. 2002, A&A, 387, 179

- Nakanishi, H. & Sofue, Y. 2006, *PASJ*, 58, 847
- Öberg, K.I., Garrod, R.T., van Dishoeck, E.F., Linnartz, H. 2009, *A&A*, 504, 891
- Pauly, T. & Garrod, R.T. 2018, *ApJ*, 854, 13
- Pickett, H.M., Poynter, R.L., Cohen, E.A., et al. 1998, *J. Quant. Spectr. Rad. Transf.*, 60, 883
- Pineda, J.L., Langer, W.D., Velusamy, T., Goldsmith, P.F. 2013, *A&A*, 554, 103
- Prantzos N. 2008, *Space Sci. Rev.*, 135, 313
- Ramírez, I., Asplund, M., Baumann, P., Meléndez, J., Bensby, T. 2010, *A&A*, 521, A33
- Reid, M.J., Menten, K.M., Brunthaler, A., et al. 2014, *ApJ*, 783, 130
- Rivilla, V.M., Beltrán, M.T., Cesaroni, R., Fontani, F., Codella, C., Zhang, Q. 2017, *A&A*, 598, 59
- Rivilla, V.M., Beltrán, M.T., Vasyunin, A., Caselli, P., Viti, S., Fontani, F., Cesaroni, R. 2019, *MNRAS*, 483, 806
- Romano, D., Franchini, M., Grisoni, V., Spitoni, E., Matteucci, F., Morossi, C. 2020, *A&A*, 639, 37
- Sewiło, M., Indebetouw, R., Charnley, S.B., Zahorecz, S., Oliveira, J.M. et al. 2018, *ApJL*, 853, L19
- Sewiło, M., Cordiner, M., Charnley, S.B., Oliveira, J.M., Garcia Berrios, E., et al. 2022, *arXiv:220109945S*
- Shimonishi, T., Watanabe, Y., Nishimura, Y., Aikawa, Y., Yamamoto, S., et al. 2018, *ApJ*, 891, 164
- Shimonishi, T., Izumi, N., Furuya, K., Yasui, C. 2021, *ApJ*, 922, 206
- Shirley, Y.L. 2015, *PASP*, 127, 299
- Spina, L., Magrini, L., Cunha, K. 2022, *Universe*, 8, 875
- Spitoni, E., Matteucci, F., Sozzetti, A. 2014, *MNRAS*, 440, 2588
- Spitoni, E., Gioannini, L., Matteucci, F. 2017, *A&A*, 605, 38
- Tielens A.G.G.M., Hagen W., 1982, *A&A*, 114, 245
- van der Tak, F.F.S., van Dishoeck, E.F., Caselli, P. 2000, *A&A*, 361, 327
- Vasyunin, A.I., Caselli, P., Dulieu, F., Jiménez-Serra, I. 2017, *ApJ*, 842, 33
- Vasyunina, T., Vasyunin, A.I., Herbst, E., Linz, H., Voronkov, M. et al. 2014, *ApJ*, 780, 85
- Viti, S., Fontani, F., Jiménez-Serra, I. 2020, *MNRAS*, 497, 4333
- Watanabe, N. & Kouchi, A. 2002, *ApJ*, 571, L173
- Wenger, T.V., Bailer, D.S., Anderson, L.D., Bania, T.M. 2019, *ApJ*, 887, 114
- Woods P.M., Kelly G., Viti S., Slater B., Brown W.A., Puletti F., Burke D.J., Raza Z. 2012, *ApJ*, 750, 19
- Woods P.M., Slater B., Raza Z., Viti S., Brown W.A., Burke D.J. 2013, *ApJ*, 777, 90

Appendix A: Spectra

We show in this appendix the spectra of CH₃OH, HCO and H₂CO analysed in this work (see Sect. 2).

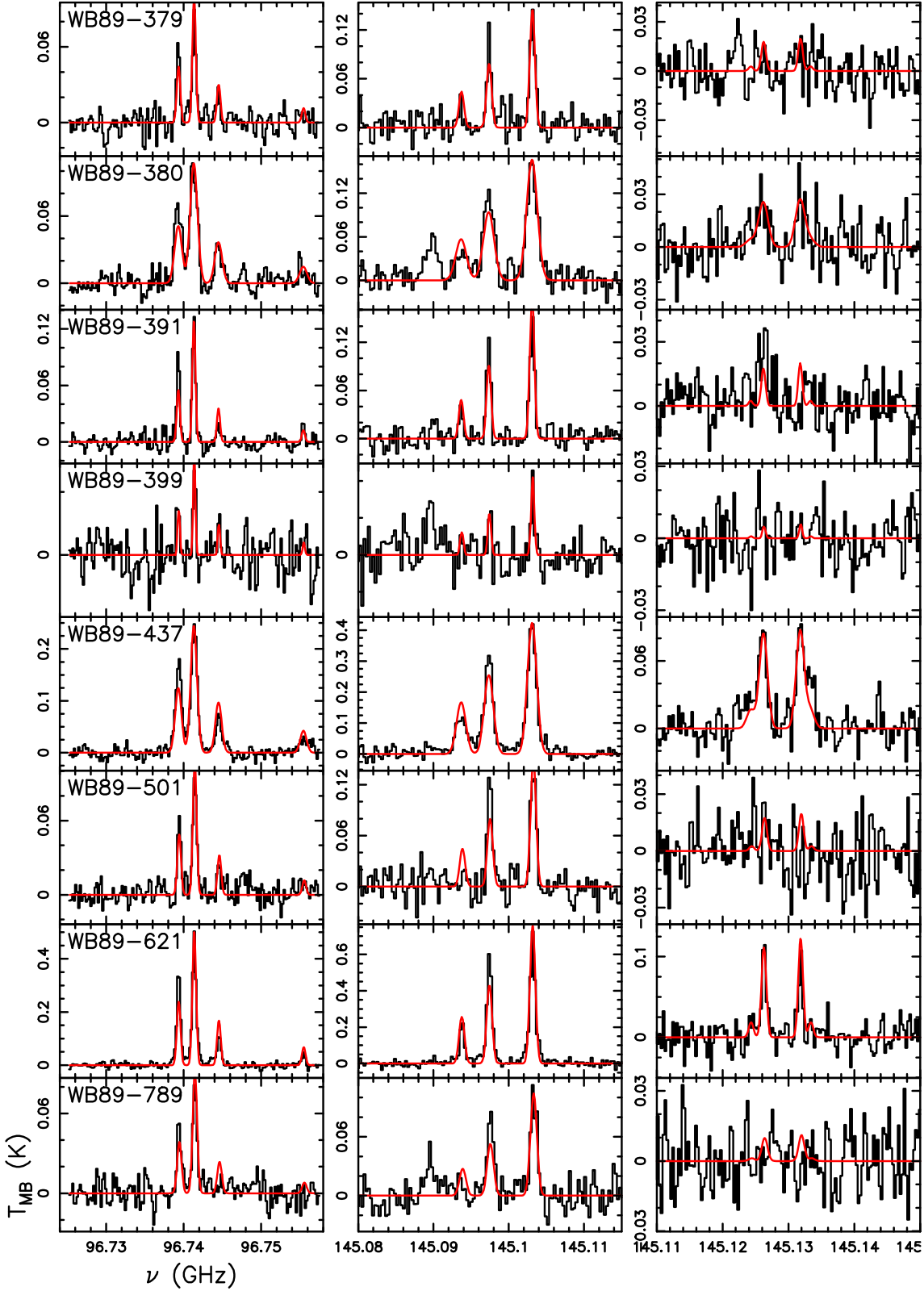


Fig. A.1. Spectra of CH₃OH lines identified in the 3 and 2 mm bands (Table 2) of the IRAM-30m telescope towards the eight first sources listed in Table 1. The red curve in each frame represents the best fit to the lines performed with MADCUBA (see Sect. 3).

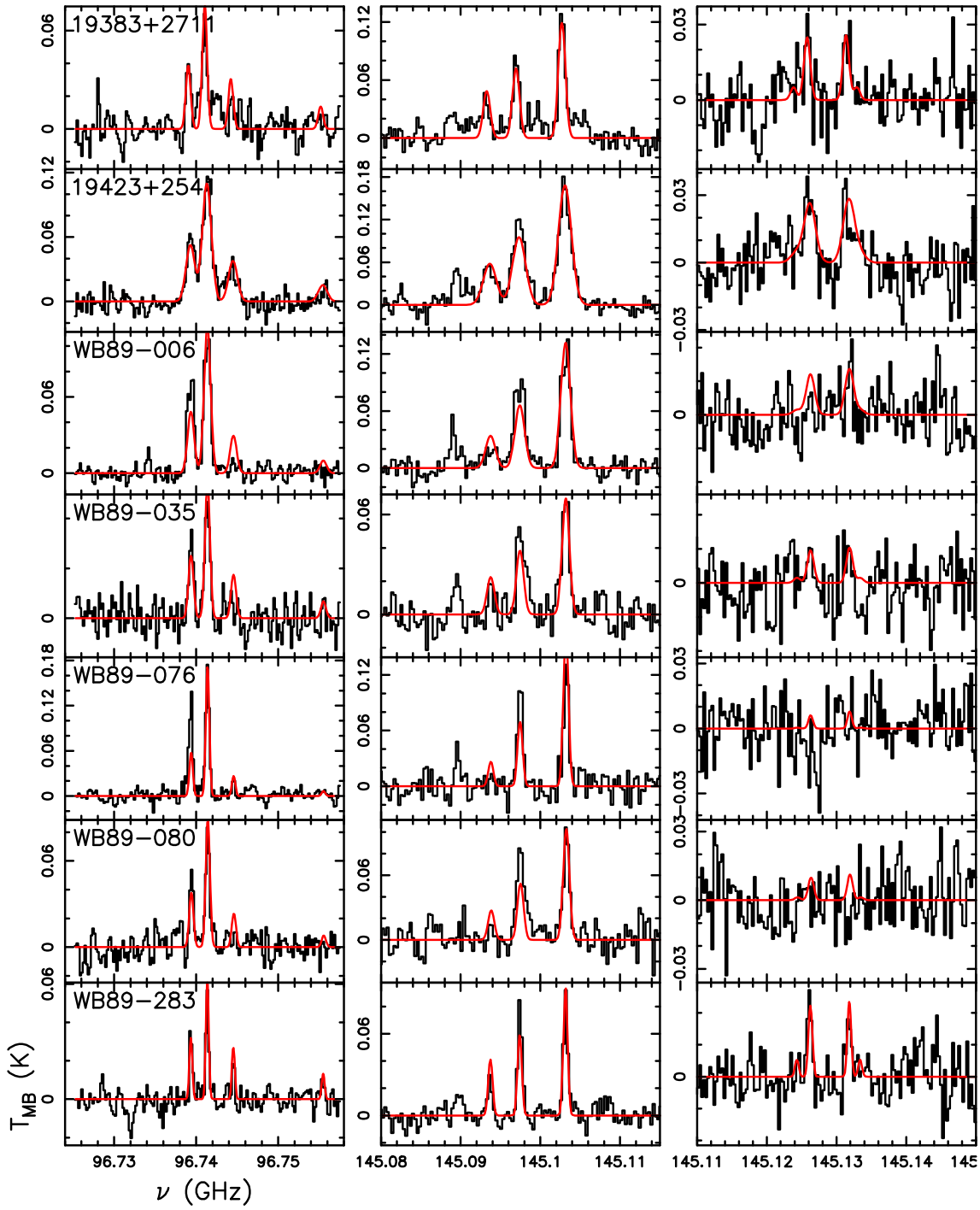


Fig. A.2. Same as Fig A.1 for the remaining seven sources.

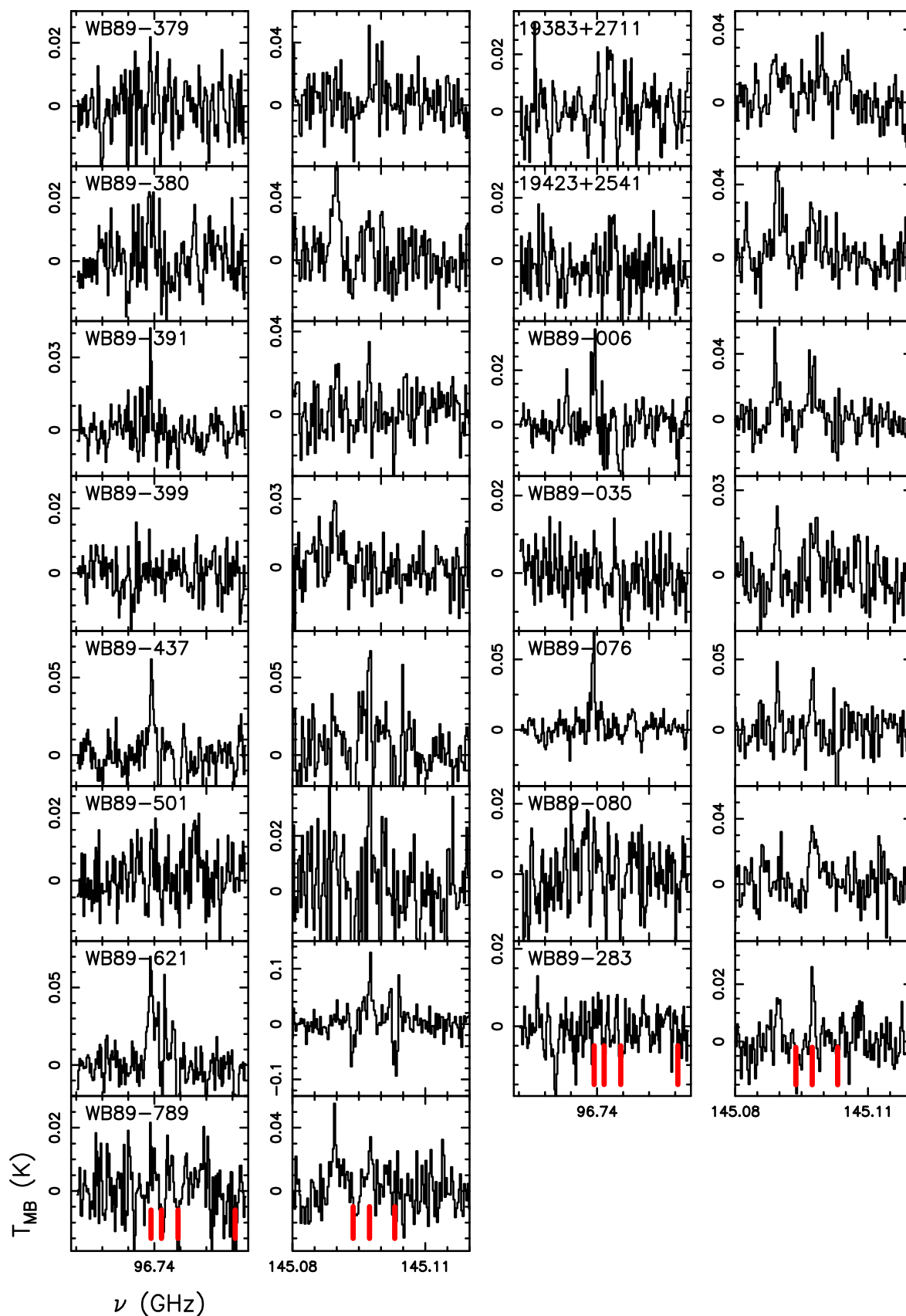


Fig. A.3. Residuals obtained from the best fits shown in Figs. A.1 and A.2. At 2 mm, we only show the residuals of the lines shown in the second panel of Figs A.1 and A.2. The frequency of the fitted lines are indicated by vertical red lines.

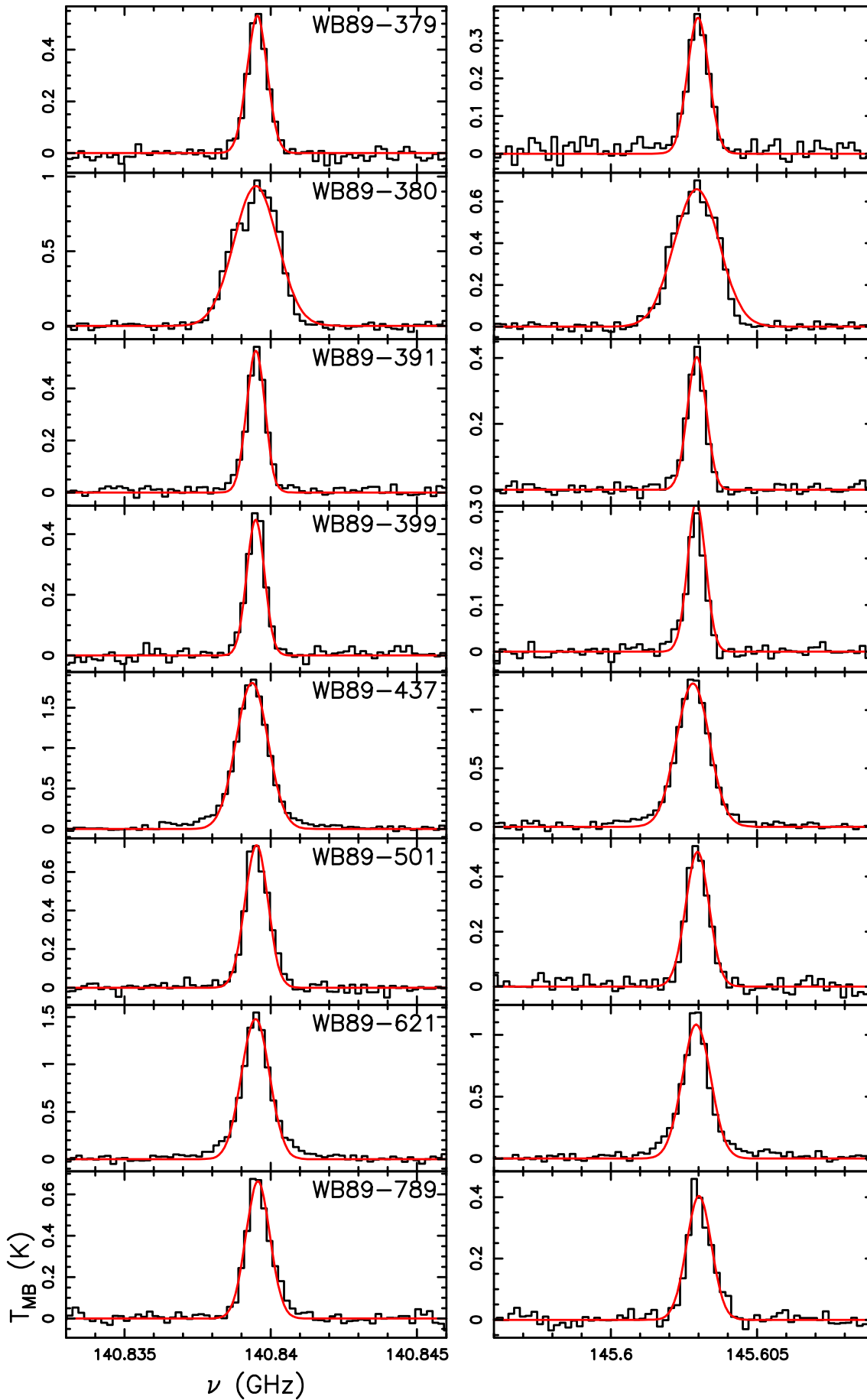


Fig. A.4. Spectra of the H₂CO lines listed in Table 2 observed at 2 mm with the IRAM-30m telescope towards the eight first sources listed in Table 1. The red curve in each frame represents the best fit to the lines performed with MADCUBA (see Sect. 3).

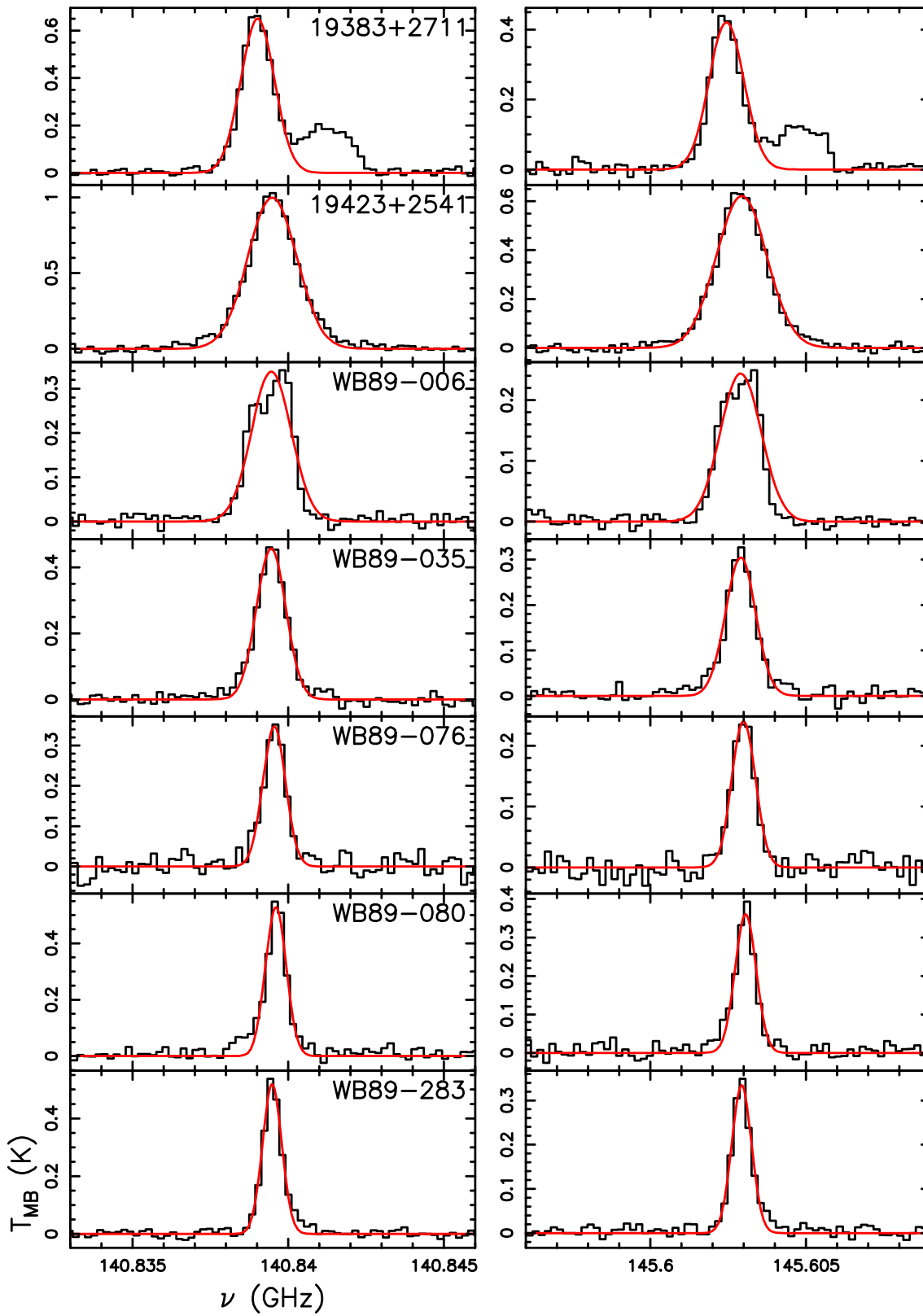


Fig. A.5. Same as Fig A.4 for the remaining seven sources.

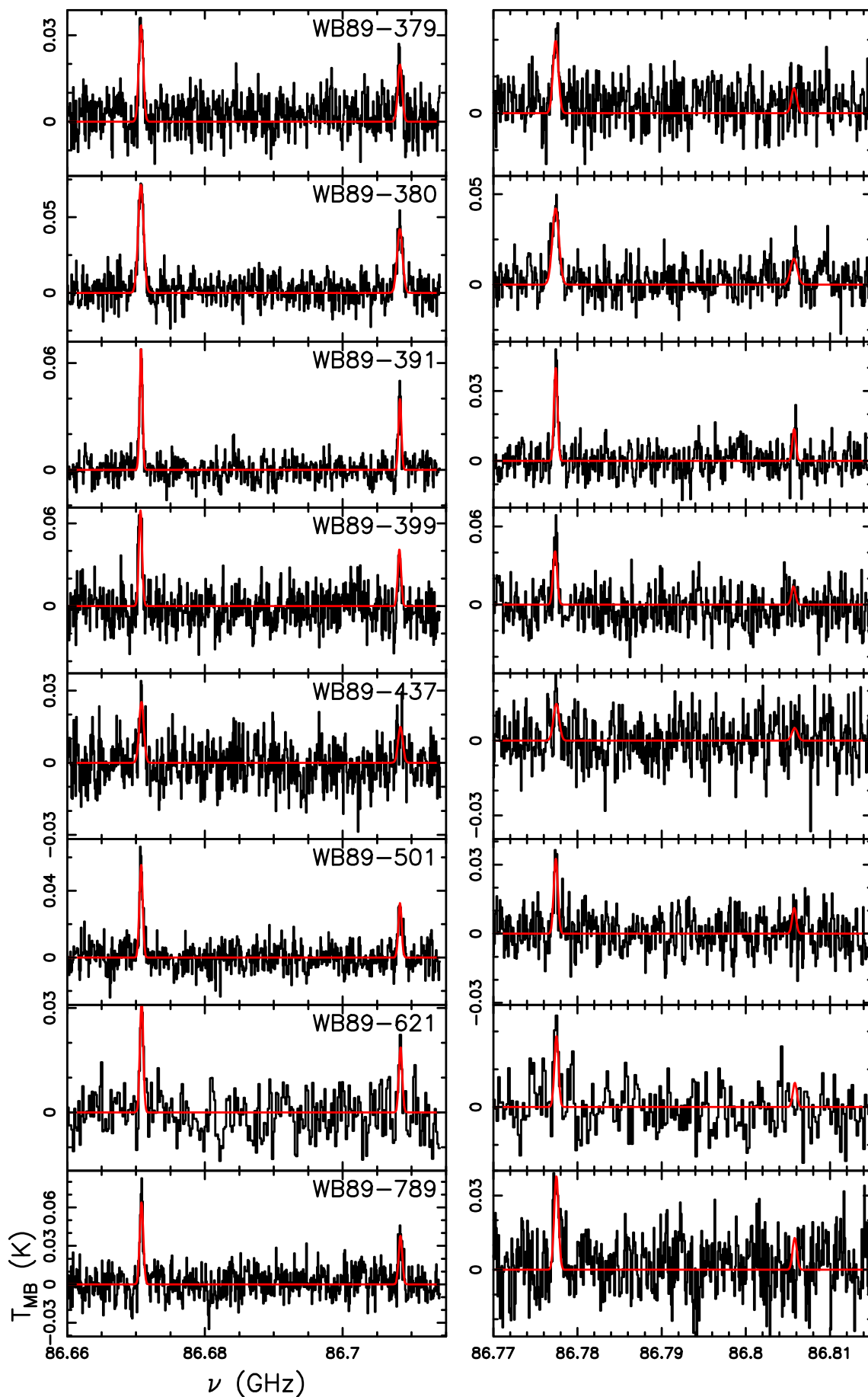


Fig. A.6. Spectra of the HCO lines listed in Table 2 observed at 3 mm with the IRAM-30m telescope towards the eight first sources listed in Table 1. The red curve in each frame represents the best fit to the lines performed with *MADCUBA* by fixing T_{ex} at the excitation temperature of CH_3OH (see Sects. 3 and 4.3).

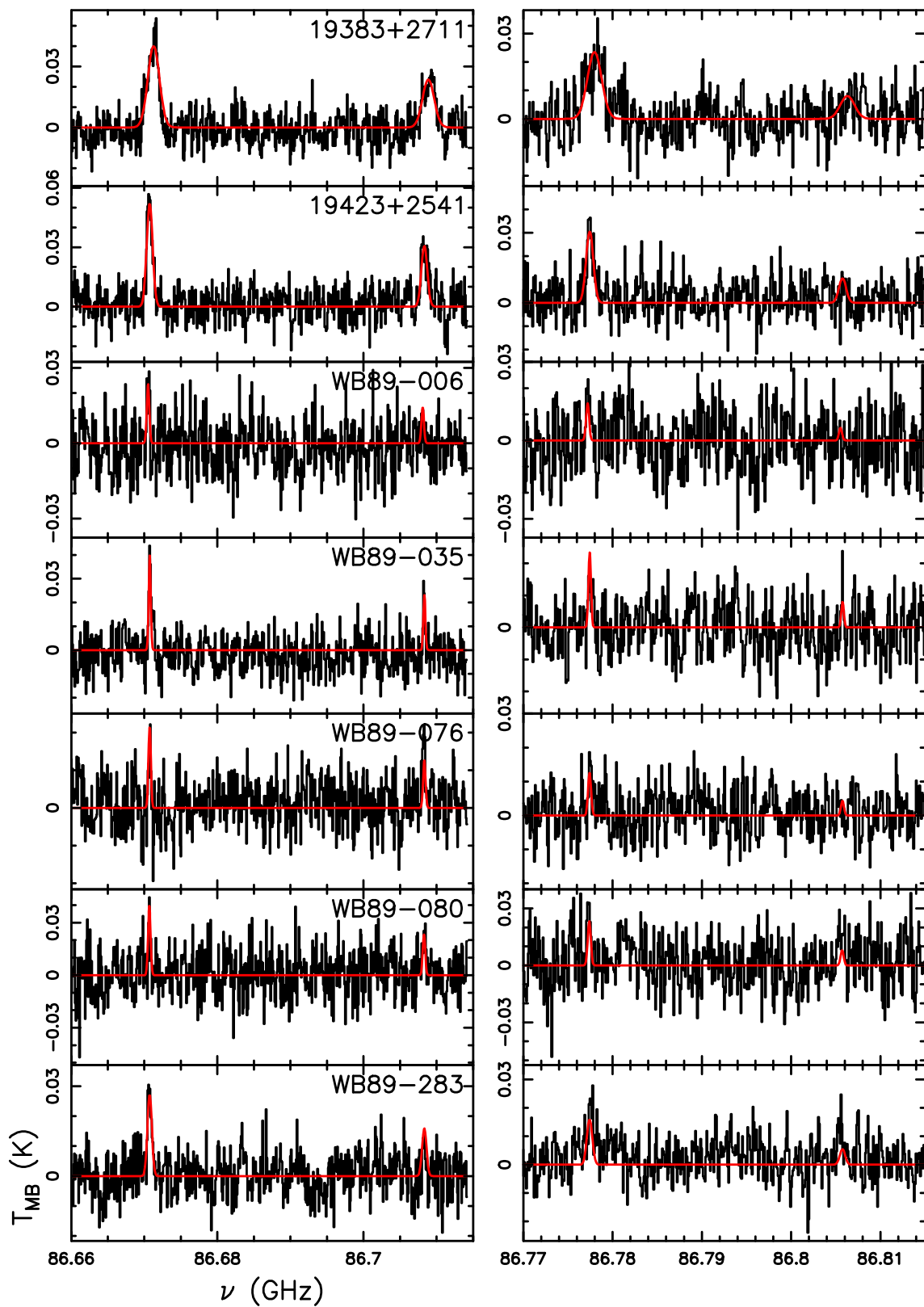


Fig. A.7. Same as Fig A.6 for the remaining seven sources.

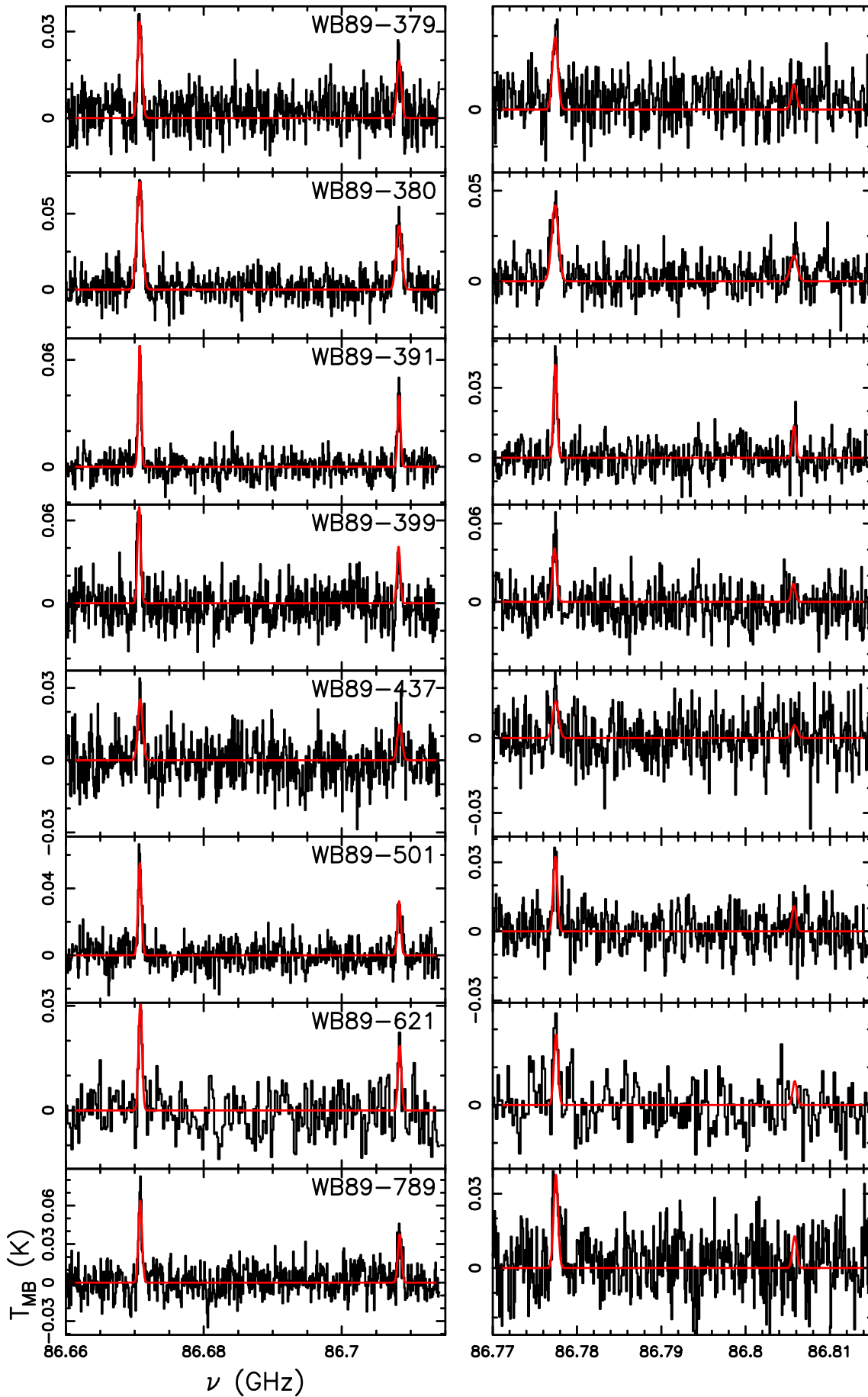


Fig. A.8. Same as Fig. A.6, with the best fit obtained with `MADCUBA` fixing T_{ex} at the excitation temperature of H_2CO (see Sects. 3 and 4.3).

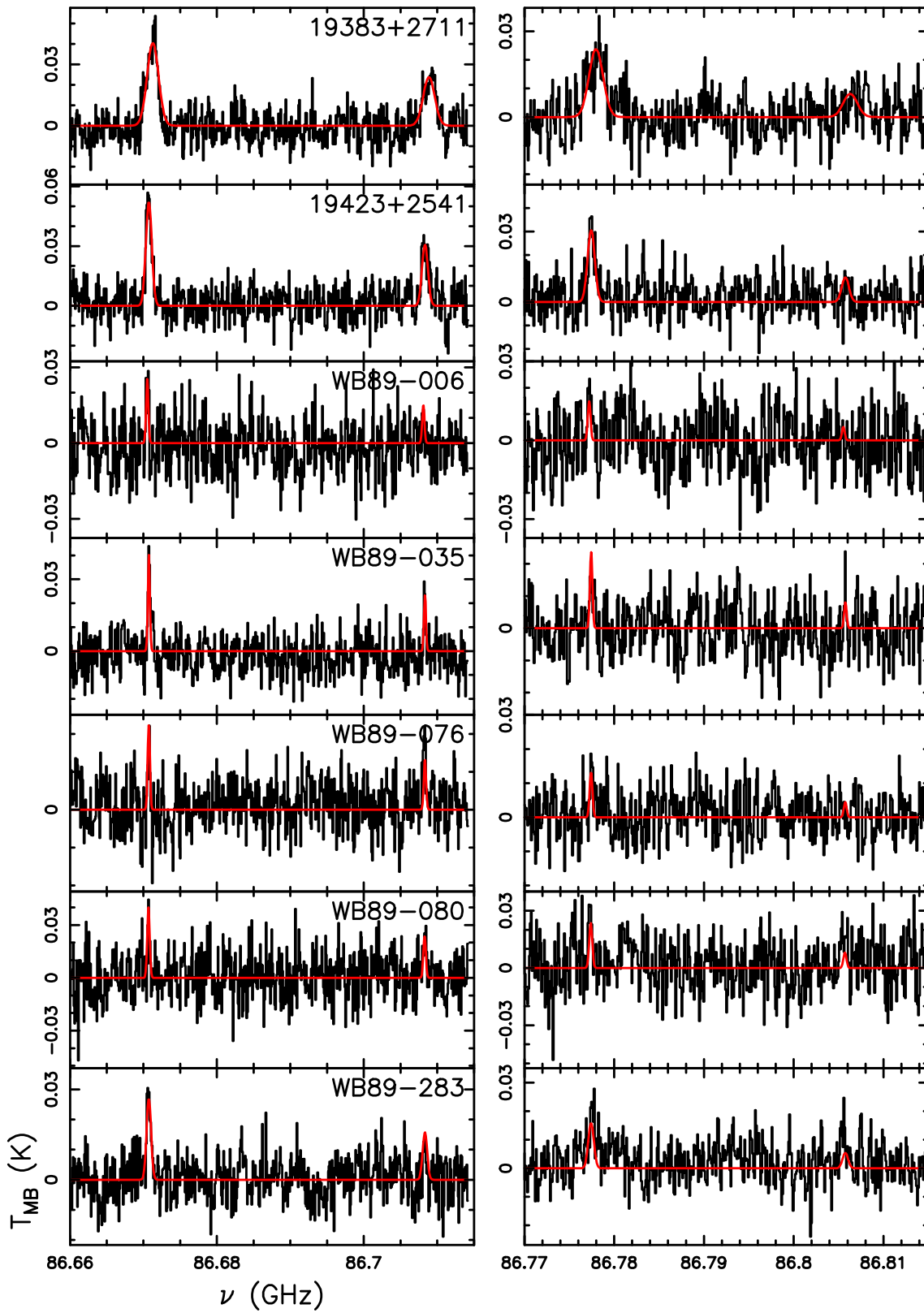


Fig. A.9. Same as Fig A.8 for the remaining seven sources.

Appendix B: Results of HCO line fitting assuming T_{ex} from H_2CO .

Fit results to the HCO lines obtained with MADCUBA fixing T_{ex} at the excitation temperature of H_2CO (see Sects. 3 and 4.3).

Table B.1. HCO line parameters.

source	$V^{(1)}$ km s $^{-1}$	FWHM $^{(1)}$ km s $^{-1}$	$N_{\text{tot}}^{(1)}$ $\times 10^{12}$ cm $^{-2}$	$T_{\text{ex}}^{(2)}$ K	$X_{\text{CO}}[\text{HCO}]^{(3)}$ $\times 10^{-10}$	$X_{\text{Her}}[\text{HCO}]^{(4)}$ $\times 10^{-10}$
WB89-379	-89.17(0.09)	2.6(0.2)	7.1(0.5)	31	11(2)	11(2)
WB89-380	-86.46(0.06)	3.2(0.1)	17.0(0.6)	28	15(2)	–
WB89-391	-85.94(0.04)	1.7(0.1)	7.1(0.4)	25	14(2)	–
WB89-399	-81.79(0.09)	2.0(0.2)	9.0(0.8)	26	14(2)	3.6(0.6)
WB89-437	-71.8(0.2)	2.8(0.4)	6.2(0.8)	33	4.5(1.0)	–
WB89-501	-58.33(0.07)	2.0(0.2)	9.8(0.7)	33	9(2)	–
WB89-621	-25.5(0.1)	2.0(0.2)	4.2(0.5)	26	3.2(0.7)	4.0(0.9)
WB89-789	34.21(0.08)	2.1(0.2)	18(1.4)	45	28(5)	16(3)
19383+2711	-68.6(0.2)	6.5(0.3)	25(1.2)	36	–	–
19423+2541	-72.54(0.09)	3.3(0.2)	19(1)	40	–	27(4)
WB89-006	-90.5(0.1)	1.4(0.3)	2.0(0.4)	26	3.1(0.8)	–
WB89-035	-77.60(0.07)	1.15(0.16)	3.0(0.4)	32	6(1)	6(1)
WB89-076	-97.1(0.1)	1.4(0.2)	2.0(0.3)	28	4.3(0.9)	7(2)
WB89-080	-74.0(0.1)	1.4(0.3)	4.3(0.7)	30	5(1)	9(2)
WB89-283	-94.4(0.14)	2.5(0.3)	6.5(0.7)	35	10(2)	42(10)

⁽¹⁾ Best fit parameters obtained with MADCUBA. We assumed that the emission fills the telescope beam;

⁽²⁾ fixed to the value obtained from H_2CO (Table 4);

⁽³⁾ fractional abundance w.r.t. H_2 from $N_{\text{CO}}(\text{H}_2)$, given in Table 1;

⁽⁴⁾ fractional abundance w.r.t. H_2 from $N_{\text{Her}}(\text{H}_2)$, given in Table 1.